Investigo
Universidade Vigo

Biblioteca Universitaria
Área de Repositorio Institucional

Tfno.: 986 813 821
investigo@uvigo.gal

This document is the Accepted Manuscript version of a Published Work that appeared in final form in *Inorganic Chemistry*, copyright © 2019 American Chemical Society after peer review and technical editing by the publisher. To access the final edited and published work see:
https://doi.org/10.1021/acs.inorgchem.9b00869

Lanthanide Complexes with 1H paraCEST and 19F Response for Magnetic Resonance Imaging Applications

Rosa Pujales-Paradela, Tanja Savić, Paulo Pérez-Lourido, David Esteban-Gómez, Goran Angelovski, Mauro Botta, and Carlos Platas-Iglesias

Inorganic Chemistry 2019 58 (11), 7571-7583
DOI: 10.1021/acs.inorgchem.9b00869

Lanthanide Complexes with ^{1}H paraCEST and ^{19}F Response for MRI applications

Rosa Pujales-Paradela,[†] Tanja Savić,[§] Paulo Pérez-Lourido,[¥] David Esteban-Gómez, [†] Goran Angelovski,*[§] Mauro Botta,[‡] Carlos Platas-Iglesias*[†]

[†] Centro de Investigacións Científicas Avanzadas (CICA) and Departamento de Química, Facultade de Ciencias, Universidade da Coruña, 15071 A Coruña, Galicia, Spain

e-mail: carlos.platas.iglesias@udc.es

[§] MR Neuroimaging Agents, Max Planck Institute for Biological Cybernetics, 72076 Tuebingen, Germany

e-mail: goran.angelovski@tuebingen.mpg.de

[¥] Departamento de Química Inorgánica, Facultad de Ciencias, Universidade de Vigo, As Lagoas, Marcosende, 36310 Pontevedra, Spain

[‡] Dipartimento di Scienze e Innovazione Tecnologica, Università del Piemonte Orientale "A. Avogadro", Viale T. Michel 11, 15121 Alessandria, Italy.

ABSTRACT: We present a detailed study of the lanthanide(III) complexes with cyclen-based ligands containing phenylacetamide pendants that incorporate CF_3 group(s) at different distances from the metal ion. The complexes exhibit square antiprismatic (SAP) coordination in solution, as demonstrated by the analysis of the Yb^{3+}-induced paramagnetic shifts and the X-ray structure of the [YbL^3] complex. Luminescence lifetime measurements and a detailed ^{1}H and ^{17}O relaxometric characterization confirmed the presence of an inner-sphere water molecule. The Tm^{3+} complexes provide Chemical Exchange Saturation Transfer (CEST) response upon saturation at the frequency of the amide protons. A ^{19}F relaxation study provided accurate estimates of the Ln···F distances that were used to rationalize the efficiency of the complexes as ^{19}F MRI probes, which was tested in vitro using MRI phantom studies.

INTRODUCTION

Fluorinated probes for application in magnetic resonance imaging (MRI) represent an interesting alternative to the classical ^{1}H contrast agents. The first in vitro ^{19}F MRI study dates from 1977, when Holland reported phantoms of NaF solutions.[1] *In vivo* ^{19}F MRI studies were reported eight years later by using fluorinated anesthetics.[2] The interest on this topic has been reinforced in the last decade, in particular with the use of perfluorocarbon molecules, often as colloidal suspensions or emulsions in aqueous buffer.[3] One of the most interesting and promising properties offered by these fluorinated systems is the absence of a background signal, as fluorine is present *in vivo* in negligible amounts, mainly as solid salts in teeth and bones.[4] Furthermore, the ^{19}F nucleus presents 100% isotopic abundance, a sensitivity only slightly lower with respect to ^{1}H (83%) and a non-quadrupolar nuclear spin (I= ½).[5] The high gyromagnetic ratio of ^{19}F (40.05 MHz·T^{-1}) is very similar to that of ^{1}H (42.55 MHz·T^{-1}), so that ^{19}F detection requires only a small tuning of the conventional MRI scanners.[6]

Another interesting class of contrast agents for application in MRI that have been intensively studied during the last two decades are chemical exchange saturation transfer (CEST) contrast agents.[7] These probes contain protons involved in slow-to-intermediate chemical exchange with bulk water. Application of a radiofrequency pulse at the frequency of the exchangeable protons results in the transference of some magnetization to bulk water through chemical exchange, so that the intensity of the bulk water signal decreases.[7,8]

The use of paramagnetic ^{19}F and CEST (paraCEST) probes has some advantages over diamagnetic ones. First, the ^{19}F relaxation times of diamagnetic compounds are relatively long, which may result in rather long acquisition times. The introduction of a paramagnetic ion in the vicinity of the ^{19}F nucleus shortens these relaxation times thanks to the paramagnetic relaxation enhancement effect.[9] This allows using ultrafast pulse sequences that shorten the acquisition times and increase the signal-to-noise ratio (SNR) of the images.[10] Following the pioneering work of Parker on paramagnetic lanthanide complexes,[11] different groups have developed ^{19}F MRI probes using either paramagnetic lanthanide[12,13] or transition metal ions (i. e. Fe^{2+}, $Co^{2+/3+}$, Ni^{2+} or Cu^{+}/Cu^{2+}).[14] ParaCEST probes also present some advantages with respect to diamagnetic derivatives, as the paramagnetic chemical shifts induced by the metal ion shift the

signal of exchangeable protons away from that of bulk water. As a result, the resonance of exchangeable protons can be saturated selectively and the slow-to-intermediate exchange condition can be achieved with faster exchange rates.[15] Dual ^{19}F/ParaCEST probes can potentially combine the advantages of the two techniques: The lack of background signal at the ^{19}F frequency and responsiveness to physiological parameters (i. e. pH) often observed for CEST agents.

Chart 1. Structures of the ligands discussed in the present work and numbering scheme used for NMR spectral assignment.

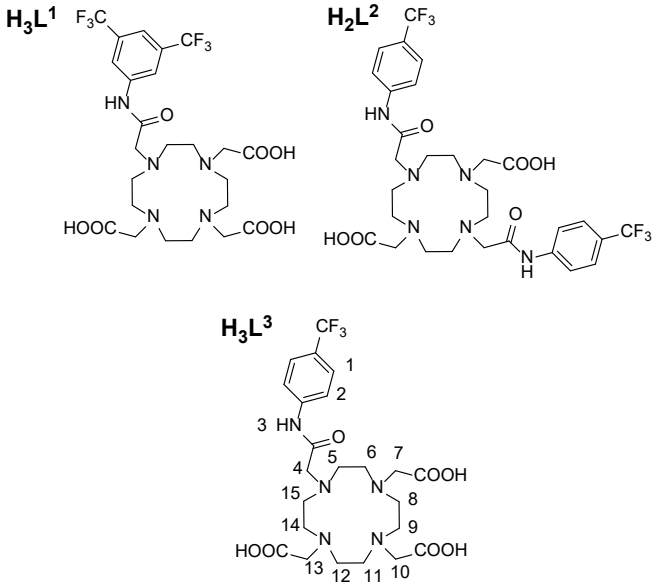

In a recent work, we have shown that the [GdL^1] and [GdL^2]$^+$ complexes (Chart 1) provide dual response at the ^{1}H and ^{19}F frequencies. The ^{1}H response is generated by the classical T_1 effect, thanks to the presence of a water molecule coordinated to the Gd^{3+} ion in fast exchange with bulk water. These complexes also showed interesting ^{19}F NMR relaxation properties, particularly in the case of [GdL^1], as the longer Gd···F distance results in slower transverse ^{19}F relaxation, and thus in sharper signals.[16] In this paper we report a detailed study of the potential of the complexes of H_3L^1 and H_2L^2 with other lanthanide ions as ^{19}F MRI probes. In addition, we present the new cyclen-based ligand H_3L^3 and the corresponding complexes with the lanthanide ions. We report a detailed study of the ^{19}F longitudinal and transverse relaxation rates (R_1 and R_2) of these systems at different fields, and analyze the effect of the effective magnetic moment (μ_{eff}) along the lanthanide series on the ^{19}F relaxation rates. Furthermore, we present a structural study of the complexes in solution by using NMR spectroscopy and DFT calculations in combination with the luminescence lifetimes of the Eu^{3+} and Tb^{3+} analogues. We also present the X-ray structure of the [YbL^3] complex and a full relaxometric characterization of [GdL^3] including ^{1}H NMRD (Proton Nuclear Magnetic Relaxation Dispersion) profiles and ^{17}O NMR measurements. Besides, we investigated the Z-spectra at different frequency fields and temperatures for the Yb^{3+} and Tm^{3+} analogues. The amide protons of the Tm^{3+} complexes give significant CEST response, which imparts dual-frequency (^{1}H/^{19}F) response to these complexes.

RESULTS AND DISCUSSION

Synthesis and structural characterization. The synthesis of H_3L^3 was achieved by alkylation of DO3A*t*Bu with 2-chloro-N-(4-(trifluoromethyl)phenyl)acetamide in acetonitrile using $NaHCO_3$ as a base. Hydrolysis of the *tert*-butyl ester groups using formic acid afforded H_3L^3 in 63% over the two steps. The complexes with different Ln^{3+} ions were prepared by reacting the ligand with the corresponding hydrated $LnCl_3$ salt in 1-butanol. The charge neutral [LnL^3] complexes (Ln = Eu, Gd, Tb, Tm Yb or Lu) were isolated in ~60-75% yields after purification using reverse-phase chromatography. The complexes of ligands H_3L^1 and H_2L^2 were prepared following the same procedures described previously for the Gd^{3+} analogues.[16]

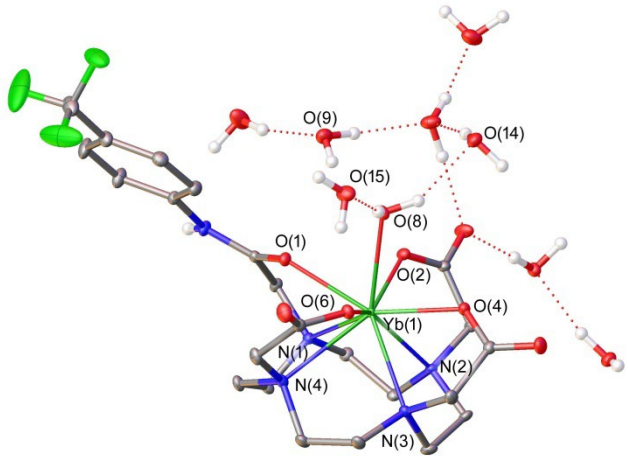

Figure 1. X-ray structure of the [YbL^3(H$_2$O)]·7H$_2$O complex. Bond distances (Å): Yb(1)··O(1), 2.3368(10), Yb(1)··O(2), 2.2725(9), Yb(1)··O(4), 2.2743(10), Yb(1)··O(6), 2.2420(10), Yb(1)··O(8), 2.4577(10), Yb(1) ·N(1), 2.6430(11), Yb(1)··N(2), 2.6098(11), Yb(1)··N(3), 2.5880(11), Yb(1)··N(4), 2.6512(11). The ellipsoids represent the 50% probability level.

The crystal structure of the [YbL^3(H$_2$O)] complex was determined by single crystal X-ray diffraction measurements (Figure 1). The asymmetric unit contains the [YbL^3(H$_2$O)] entity and seven water molecules of crystallization. The four amine donor atoms of the macrocycle and the four oxygen atoms of the carbonyl groups provide an eight coordination environment to the metal ion, while the ninth coordination is completed by a water molecule. The coordination polyhedron around the Yb^{3+} ion can be described as capped square antiprism (SAP). The nitrogen atoms of the cyclen unit define the lower plane of the polyhedron, the oxygen atoms of the pendant arms the upper plane, and the oxygen atom of the coordinated water molecule occupies the capping position. The metal ion is placed closer to the upper plane (0.726 Å) than to the plane delineated by the nitrogen atoms (1.595 Å), a general trend observed for the family of lanthanide DOTA derivatives.[17] The mean twist angle of the two square planes is 39.8 $\pm$ 1.0º, a value that is close to that expected for an ideal square antiprism (45º). The crystal lattice contains the two centrosymmetrically related $\Delta(\lambda\lambda\lambda\lambda)/\Lambda(\delta\delta\delta\delta)$ enantiomers, where Λ and Δ define the two possible orientations of the four pendant arms (clockwise or anti-clockwise) with

respect to the C_4 pseudo-symmetry axis of the complex, while δ or λ describe the conformations of the five-membered chelate rings resulting from the coordination of the ethylenediamine units.[18] The cyclen unit adopts a [3333] conformation using the notation proposed by Dale.[19] The Yb-N distances are close to those observed for nine-coordinated Yb^{3+} complexes with cyclen based ligands (2.58-2.64 Å).[17,20-21] The bond distance involving the coordinated water molecule [Yb(1)···O(8), 2.4577(10) Å] is longer than those reported for Yb^{3+} DOTA-tetraamide complexes, which present a rather broad range (2.34-2.44 Å).[21] The longer distance observed for [$YbL^3(H_2O)$] is related to the reduced positive charge of the complex, which weakens the Yb-O_{water} interaction.[22]

The coordinated water molecule is involved in hydrogen-bonding interactions with up to three second-sphere water molecules. The coordinated water molecule serves as a hydrogen bond donor to O(15) and O(14) [O(8)···O(15) = 2.7716(11) Å, O(8)-H(8D)···O(15) = 1.93 Å, O(8)-H(8D)···O(15) = 159.6º; O(8)···O(14) = 2.8377(12) Å, O(8)-H(8C)···O(14) = 2.04 Å, O(8)-H(8C)···O(14) = 149.8º;]. A weaker hydrogen bond involves a third water molecule of crystallization acting as a hydrogen bond donor [O(9)···O(8) = 3.0350(11) Å, O(9)-H(9D)···O(8) = 2.25 Å, O(9)-H(9D)···O(8) = 159.0º] and the inner-sphere water molecule. Similar hydrogen bonding patterns were observed in the solid state for several Gd^{3+} complexes in the presence of counterions with poor ability to form hydrogen bonds.[23] Similar second-sphere interactions were also found to be crucial to obtain accurate Gd-O_{water} distances and ^{17}O spin densities for Gd^{3+} complexes using DFT methods.[24]

The emission spectra of the [LnL^3] complexes (Ln = Eu, Tb) recorded under excitation through the ligand bands at 263 nm present the expected $^5D_0 \rightarrow {}^7F_J$ transitions of Eu^{3+} (J = 0-4) or $^5D_4 \rightarrow {}^7F_J$ transitions of Tb^{3+} (Figures S15-S16, Supporting Information). The emission lifetimes of $^5D_0$ (Eu) and $^5D_4$ (Tb) excited states recorded in H_2O and D_2O solutions (Table 1) provide hydration numbers that confirm the presence of a water molecule in the first coordination sphere of the metal ions.[25] Both the lifetimes and emission spectra of [LnL^1] and [LnL^3] are very similar (Figure S15 Supporting Information), which points to very similar structures of these complexes in solution. This implies that the different substitution pattern of the phenylacetamide pendant arm of these ligands does not affect significantly the structure of the corresponding complexes. The emission spectrum of $[EuL^2]^+$ differs significantly from those of [EuL^1] and [EuL^3], particularly in the relative intensity of the ΔJ = 1, 2 and 4 transitions, and the shape of the ΔJ = 1 transition. The lifetimes of [EuL^1] and [EuL^3] recorded in H_2O are slightly shorter than that of $[EuL^2]^+$, a situation that is reversed in D_2O.[16]

Table 1. Emission lifetimes and hydration numbers obtained for the [EuL^3] and [TbL^3] complexes.

	τ(H_2O) / ms	τ(D_2O) / ms	q^a
EuL^3	0.616	1.904	0.9
TbL^3	1.85	3.15	0.8

[a] Obtained using the method proposed by Beeby, ref. 25.

The ^1H NMR spectra of the [EuL^3] and [YbL^3] (pD= 6.8, 10 mM, 25 ºC) present four resonances due to the most shifted axial protons of the cyclen unit in the range ~29 – 34 ([EuL^3]) and 109 – 126 ppm ([YbL^3]). These chemical shifts are characteristic of complexes adopting capped square antiprismatic (SAP) coordination.[26,27] The signals of the twisted square antiprismatic isomers (TSAP) are not observed in any of the spectra, indicating that these complexes exist in solution as the SAP isomers almost exclusively.

A more detailed analysis of the structure of the [YbL^3] complex in solution was carried out by analyzing the Yb^{3+}-induced pseudocontact shifts. The ^1H NMR spectrum of [YbL^3] presents 26 well-resolved signals that could be assigned in part with the aid of ^1H-^1H COSY spectra and line-width analysis. This provides a straightforward differentiation of the broad axial signals from the sharper equatorial ones, as a result of their different distances to the paramagnetic ions.[28]

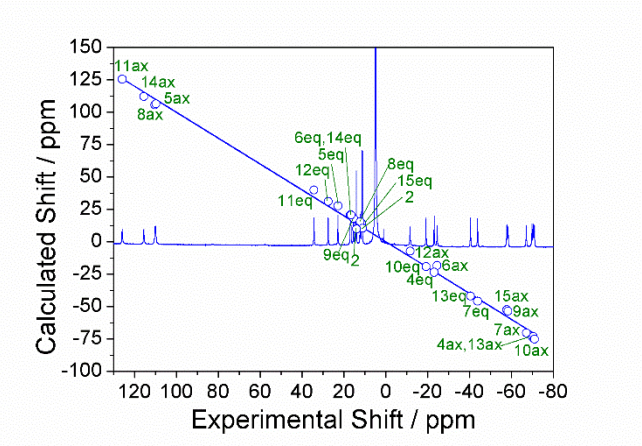

Figure 2. ^1H NMR (300 MHz, 298 K) spectrum of [YbL^3] recorded in D_2O solution and plot of the experimental shifts versus those calculated with the X-ray structure and pseudocontact contributions. The solid line represents the identity line.

The ^1H paramagnetic shifts induced by Yb^{3+} are dominated by the pseudocontact mechanism, with contact contributions being generally negligible.[29] The pseudocontact shifts can be expressed as linear combinations of the axial and rhombic components of the susceptibility tensor χ (Eq (1) and (2), respectively):[30]

$$\delta^{pc} = \frac{1}{2N_A}\left[(\chi_{zz} - \chi_{av})\left(\frac{3z^2-r^2}{r^5}\right) + (\chi_{xx} - \chi_{yy})\left(\frac{x^2-y^2}{r^5}\right)\right] \quad (1)$$

$$r = \sqrt{x^2 + y^2 + z^2} \quad (2)$$

The paramagnetic shifts of [YbL^3] were analyzed by assuming diamagnetic shifts of 7.8 ppm for the signals of aromatic protons and 3.0 ppm for CH_2 protons. The paramagnetic shifts were then fitted to Eq (1) by using the Cartesian coordinates obtained from the X-ray structure described above. Since the positions of the magnetic axes are not constrained by symmetry for this complex, we carried out a fitting procedure involving five parameters: the axial (χ_{zz} - χ_{av}) and rhombic (χ_{xx} - χ_{yy}) magnetic anisotropies and the three Euler angles that allow the

rotation of the complex, so that the Cartesian axes match the magnetic axes.[31] The best fit of the data provided calculated pseudocontact shifts in good agreement with the experimental values (Figure 2, see also Table S2, Supporting Information), with deviations < 6.1 ppm. The calculated axial and rhombic magnetic susceptibilities are $\chi_{zz} - \chi_{av} = 1.34(2)$ and $\chi_{xx} - \chi_{yy} = -0.51(5)$ cm^3 K mol^{-1}, indicating that the magnetic anisotropy is dominated by the axial contribution. The orientation of the molecule that results from the analysis is such that the z magnetic axis is perpendicular to the best plane defined by the nitrogen donor atoms of the macrocycle, and contains the Yb^{3+} ion and the oxygen atom of the coordinated water molecule. Thus, the analysis of the Yb^{3+} induced shifts shows that the [YbL^3] complex retains in solution the structure observed in the solid state.

DOSY (diffusion-ordered NMR spectroscopy) experiments were performed on 15 mM H_2O solutions of [TmL^3] and selected complexes of L^1 and L^2 ([EuL^2], [TmL^1] and [YbL^1], the latter using 5 mM concentration). These experiments provided diffusion coefficients D at 298 K of $3.94(2) \times 10^{-10}$ m^2 s^{-1} for [EuL^2]$^+$, $4.65(1) \times 10^{-10}$ m^2 s^{-1} for [TmL^1], $4.82(1) \times 10^{-10}$ m^2 s^{-1} for [YbL^1] and 4.94×10^{-10} m^2 s^{-1} for [TmL^3]. The diffusion coefficients obtained for the complexes of L^1 and L^3 are very similar, as would be expected given their similar size and neutral charge. The D^{298} value determined for [EuL^2]$^+$ is somewhat lower, which is explained by the larger hydrodynamic radius associated to its higher molecular weight and positive charge. Nevertheless, the diffusion coefficients measured for these complexes are similar to those reported for lanthanide complexes with similar size,[32] and higher than the D^{298} value reported for lanthanide DO3A derivatives that form stable dimeric species in solution[33] (for comparative purposes the D^{298} values measured in D_2O must be scaled by a factor of 1.24 to account for the different viscosities of H_2O and D_2O). Thus, we conclude that the complexes investigated here adopt discrete mononuclear structures in H_2O solution.

^{1}H relaxivity and ^{17}O NMR studies. In a previous work, we reported a detailed characterization of the [GdL^1] and [GdL^2]$^+$ complexes using ^{1}H Nuclear Magnetic Relaxation Dispersion (NMRD) and ^{17}O NMR studies.[16] For the sake of completeness, we report here the characterization of [GdL^3] using the same techniques.

The relaxivity of [GdL^3] was first assessed at 298 K and 300 MHz from aqueous solutions buffered at pH 7.4 (50 mM HEPES). ^{1}H relaxivities are a measure of the efficiency of a given paramagnetic probe to enhance the relaxation of water proton nuclei, normalized to a 1 mM concentration of the paramagnetic agent. A paramagnetic relaxation enhancement with a set of Gd^{3+} solutions (concentration range 2.5-4.5 mM) resulted in a linear dependence of the relaxation rate ($R_1=1/T_1$) on the amount of the used metal ion. The slope of the straight line provided a relaxivity of $r_{1p} = 4.27$ mM^{-1} s^{-1} (Figure S13, Supporting Information), which is in perfect agreement with the expected values for small monohydrated gadolinium complexes.[34]

A more detailed information of the parameters that control the relaxivity of [GdL^3] was obtained by measuring ^{1}H NMRD profiles at 10, 25 and 37 ºC in the range from 0.01 to 70 MHz proton Larmor frequencies (Figure 3). Furthermore, ^{17}O NMR transverse relaxation rates (T_{2r}) and chemical shifts ($\Delta\omega_r$) were recorded to get insight into the exchange rate of the coordinated water molecule (k_{ex}^{298}).

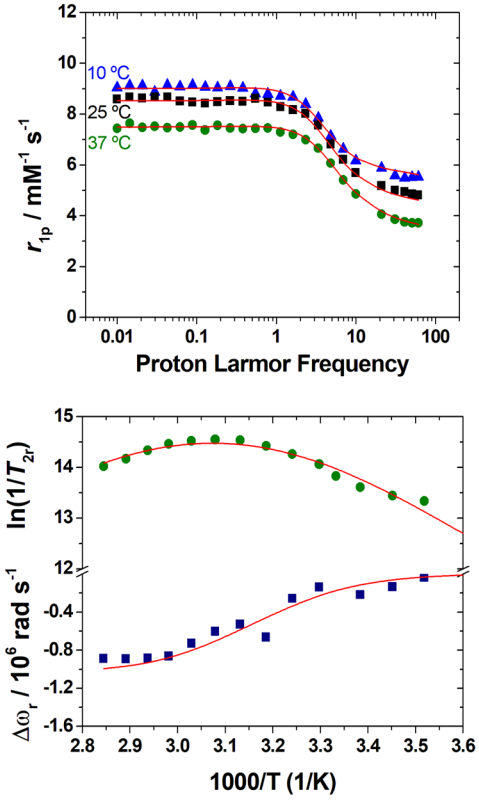

Figure 3. Top: ^{1}H NMRD profiles recorded at different temperatures for [GdL^3]. Bottom: Reduced transverse ^{17}O relaxation rates (green •) chemical shifts (blue ■) measured for [GdL^3] at 11.75 T. The lines represent the fit of the data as explained in the text.

The relaxivities of [GdL^3] present a trend similar to those of [GdL^1], showing a plateau at low fields (< 1 MHz), a sizeable dispersion in the range 1-20 MHz, reaching again another reasonably constant plateau above 21 MHz. The relaxivity decreases when the temperature is increased, which indicates that r_{1p} is limited by a fast rotation of the complex in solution characterized by a short rotational correlation time (τ_R).[35,36] The ^{17}O data obtained for [GdL^3] parallel those reported previously for [GdL^1], indicating that these complexes present similar exchange rates of the coordinated water molecule.

Table 2. Parameters obtained from the simultaneous analysis of ^{17}O NMR and ^{1}H NMRD data.

	[GdL^3]	[GdL^1] [b]	[GdL^2]$^+$ [b]	[GdDOTA]$^-$ [c]

r_{1p} at 25/37 ºC / mM^{-1} s^{-1} [b] (20 MHz)	5.18/4.07	4.97/4.14	4.26/4.23	4.7/3.8
k_{ex}^{298}/10^6 s^{-1}	1.61 ± 0.18	1.52 ± 0.17	0.73 ± 0.04	4.1
$\Delta H^{\ddagger}$ / kJ mol^{-1}	48.6 ± 1.3	49.6 ± 3.5	22.9 ± 2.0	49.8
τ_R^{298} / ps	93.4 ± 4	98.3 ± 2.8	94.0 ± 2	77
E_r / kJ mol^{-1}	19.2 ± 1.3	15.6 ± 1.1	15.6[a]	16.1
τ_v^{298}/ ps	26.5 ± 0.5	24.4 ± 2.0	15.4 ± 0.4	11
E_v / kJ mol^{-1}	1.0[a]	1.0[a]	1.0[a]	1.0[a]
D_{GdH}^{298} / 10^{-10} m^2 s^{-1}	21.8 ± 0.08	24.4 ± 0.1	24.4[a]	22
E_{DGdH}/ kJ mol^{-1}	17.9 ± 1.5	24.5 ± 3.5	15.3± 0.8	20.2
Δ^2 / 10^{19} s^{-2}	2.5 ± 0.4	2.9 ± 0.3	7.4 ± 0.4	1.6
$A/\hbar$ / 10^6 rad s^{-1}	-4.5 ± 0.3	-4.1 ± 0.3	-3.8 ± 0.3	-3.7
r_{GdH} / Å	3.1[a]	3.1[a]	3.1[a]	Or
a_{GdH} / Å	4.0[a]	4.0[a]	4.0[a]	3.5[a]
q^{298}	1[a]	1[a]	1[a]	1[a]

[a] Parameters fixed during the fitting procedure. [b] Data from reference 16. [c] Data from reference 40.

Table 3. Parameters obtained from the analysis of CEST spectra recorded at 7.05 T (complex concentration 15 mM, saturation time 10 s).

	pH	T / ºC	δ / ppm	M_z/M_0 / % (B_1 = 10 μT)	M_z/M_0 / % (B_1 = 30 μT)	r_{1p} / mM^{-1} s^{-1} [b]	k_{ex} / kHz [c]
[TmL^3]	6.9	25	-52	6	9	0.10	1.4 ± 0.3
		37	-49	9	16	0.08	3.7 ± 0.8
[YbL^3]	7.3	25	-10	22	-	0.02	4.1 ± 0.2
[TmL^1]	7.6	25	-48	5	21	0.10	12.9 ± 1.2
		37	-42	2	13	0.08	22.7 ± 2.6
[TmL^2]$^+$ [a]	7.0	25	-21	12	26	0.15	4.6 ± 1.5
		37	-24	6	-	0.15	4.9 ± 0.5

[a] Complex concentration was 8 mM. [b] Proton relaxivity of the bulk water signal. [c] Exchange rate values obtained using the Bloch-McConnell (BM) equations and assuming a 2-pool model (bulk water and THE paramagnetically-shifted exchanging pools).

The simultaneous fitting of the ^{17}O NMR and ^{1}H NMRD data of [GdL^3] was carried out using the Swift-Connick equations for the ^{17}O transverse relaxation and chemical shift data[37] and the Solomon-Bloembergen-Morgan theory[38] and Freed's model[39] for the inner- and outer-sphere contribution to relaxivity, respectively. For this analysis, the distance between the Gd^{3+} ion and the H atoms of the coordinated water molecule (r_{GdH}), the distance of closest approach for the outer-sphere contribution (a_{GdH}) and the activation energy for the modulation of the zero field splitting interaction (E_v) were fixed to common values (Table 2).[40] Figure 3 presents the fitted curves, which reproduce well the experimental data. The rotational correlation times (τ_R^{298}) and the value for the scalar hyperfine coupling constant ($A/\hbar$) obtained from the fittings of the data are in good agreement with the typical range of values observed for small Gd^{3+} complexes, supporting the consistency of the analysis. The mean square zero-field-splitting energy (Δ^2) and its correlation time (τ_v), parameters which define the relaxation of the electron spin, corroborate the aforementioned analysis, with values comparable to those determined for Gd^{3+} complexes of DOTA derivatives.[40] The same holds for the diffusion coefficient D_{GdH}^{298} and its activation energy E_{DGdH}, which are close to the values determined for the self-diffusion of water ($D_{H_2O}^{298}$ = 23.0 × 10^{-10} m^2 s^{-1} and E_{DH_2O} = 17.6 kJ mol^{-1}).[41]

The water exchange rate determined for [GdL^3] (k_{ex}^{298} = 1.61 × 10^6 s^{-1}), is virtually identical to that determined for [GdL^1] (k_{ex}^{298} = 1.5 × 10^6 s^{-1}), confirming the qualitative analysis described above. These water exchange rates are intermediate between those of the positively charged [GdL^2]$^+$ and negatively charged [GdDOTA)]$^-$.[40] This is expected considering that water exchange in these complexes follows a dissociative mechanism. Thus, an increase in the positive charge of the complex increases the activation energy to reach the eight-coordinated transition state by strengthening the Gd-O$_{water}$ bond.[42] DFT calculations provide Gd-O$_{water}$ distances of 2.428 Å for [GdL^2]$^+$ and 2.462 Å for [GdL^3] (see computational details below), which supports that the slower exchange rate of [GdL^2]$^+$ is related to a stronger Gd-O$_{water}$ bond.[22]

CEST properties. Chemical exchange saturation transfer studies were first performed for the [YbL^3] and [TmL^3] complexes (Figure 4 and Figure S25, Supporting Information). CEST spectra were acquired from 15 mM solutions at 25 and 37 ºC by applying different radiofrequency fields (B_1 = 2.5, 5, 10, 15, 20, 25 and 30 μT). The Z-spectra were performed employing a saturation time of 10 s and a 1 ppm frequency resolution. The spectrum obtained for [YbL^3] at 25 ºC presents a CEST peak at -10 ppm that is better defined at lower saturation

powers. This chemical shift is characteristic of amide protons of Yb^{3+} DOTA-monoamide derivatives,[43] and similar to that observed for DOTA-tetraamides (~-15 ppm).[20b] The CEST effect is hardly visible at 37 ºC due to the broadening of both the water and amide signals. The [TmL^3] complex presents a better defined CEST feature at ~-50 ppm that is well defined at both 25 and 37 ºC, regardless the saturation power applied. This chemical shift is similar to those observed for DOTA-tetraamide Tm^{3+} complexes.[44]

The CEST properties of [TmL^2]$^+$ and [TmL^1] complexes were also investigated under analogous conditions (Table 3, see also Figure S25, Supporting Information). The [TmL^1] complex presents CEST properties comparable to those of [TmL^3], providing a CEST peak a similar frequency. This was expected in light of their very similar structures. However, exchange rate values (k_{ex}) determined with the Bloch-McConnell (BM)[45] equations and assuming a 2-pool model (bulk water and one paramagnetically-shifted exchanging pool) were found to be very different (Table 3). Indeed, the exchange rate of amide protons was found to be one order of magnitude faster for [TmL^1] compared to [TmL^3]. This is attributed to the combined electron withdrawing effect of two $-CF_3$ groups in [TmL^1], which increases the acidity of amide protons. Since amide exchange follows a base-catalyzed mechanism,[46] an increasing acidity of amide protons is expected to result in faster exchange.

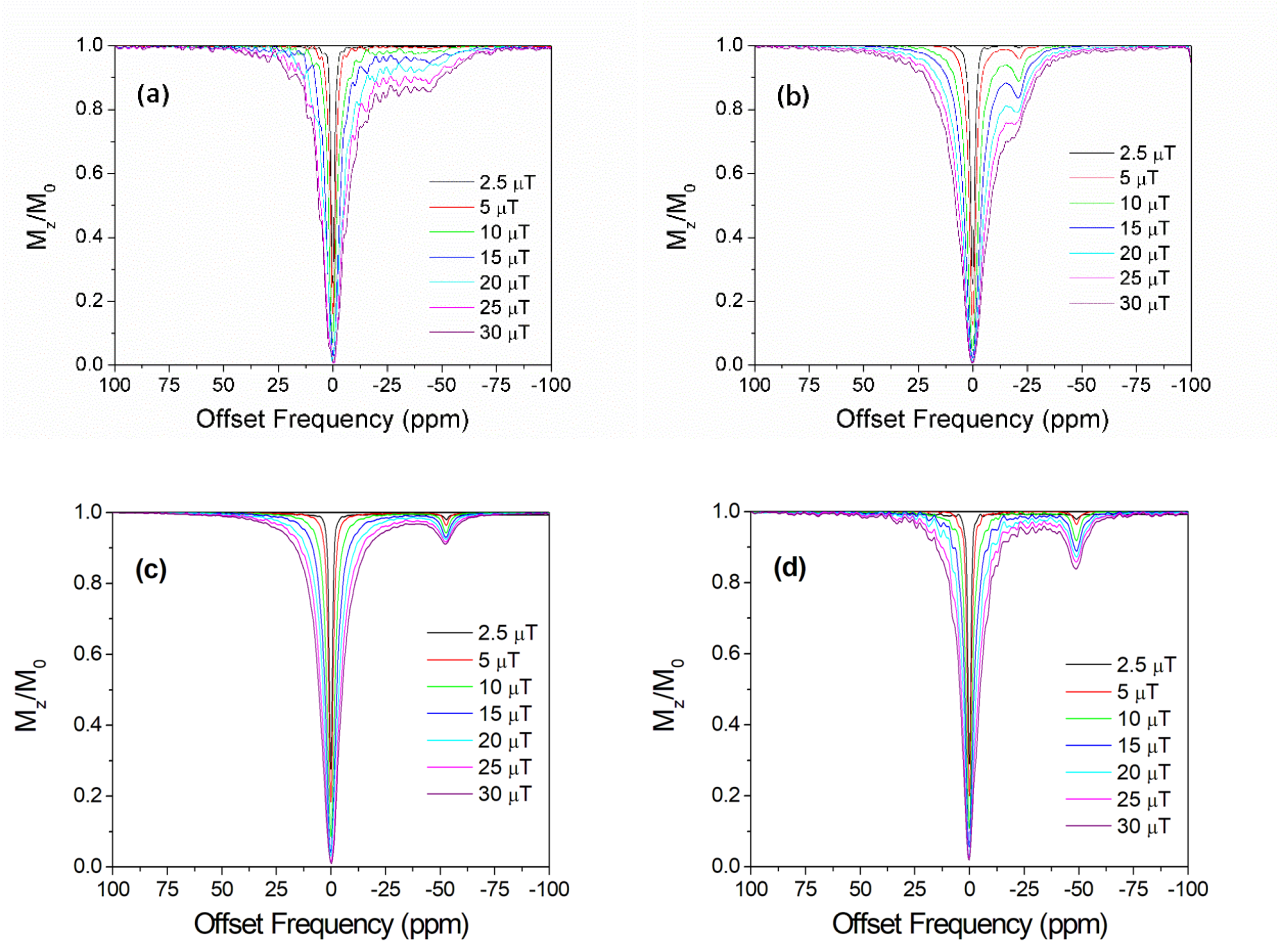

Figure 4. Upper panel: Z-spectra (saturation time 10 s) recorded for [TmL^2] (8 mM in H_2O, pH 7.2) at 25 ºC (a) and 37 ºC (b). Lower panel: Z-spectra (saturation time 10 s) recorded for [TmL^3] (15 mM in H_2O, pH 6.9) at 25 ºC (c) and 37 ºC (d).

The bis-amide [TmL^2]$^+$ complex presents a somewhat different behavior, as it shows a CEST peak with a considerably smaller shift with respect to bulk water (-21 ppm at 25 ºC, Figure 4). Since the paramagnetic shifts induced by Tm^{3+} are dominated by pseudocontact contributions,[47] this different chemical shifts observed for this complex must be related to a different magnetic anisotropy of the system.[48] The exchange rates of amide protons are only slightly higher than those reported for [TmL^3], which contains the same number and position of CF_3 groups in the amide pendant arm. However, the CEST peaks are much better resolved for [TmL^3] than for [TmL^2] due to the reduced chemical shift difference between the amide resonance and the bulk water signals in the latter.

^{19}F longitudinal and transverse relaxation rates. To assess the effect of the effective magnetic moment of various lanthanide complexes on the ^{19}F relaxation times, ^{19}F NMR chemical shifts, longitudinal and transverse relaxation data were measured for [LnL^1], [LnL^2]$^+$ and [LnL^3] at different fields (7.05, 9.4 and 11.74 T, Ln = Eu, Gd, Tb, Tm, Yb or Lu). In the case of the [LnL^1] complexes additional data at 1.43 T could be also recorded (in the remaining cases lower solubility and/or number of ^{19}F nuclei prevented relaxation measurements at low field). The observed ^{19}F NMR chemical shifts and longitudinal (R_1) and transverse (R_2) relaxation rates are compiled in Table 4.

The ^{19}F NMR spectra along the series of lanthanides present a single and intense resonance due to the CF_3 group or groups of the three ligands. The presence of a major single ^{19}F signal demonstrates the presence of a single isomer in solution (the SAP isomer). The observed ^{19}F chemical shifts (δ^{obs}) follow rather well the trend predicted by Bleaney's theory (Figure S21, Supporting Information), as they are proportional to the Bleaney constants.[9] This indicates that contact contributions are negligible, as expected for remote nuclei with respect to the paramagnetic center (in terms of number of bonds). The slope of the straight line obtained for [LnL^1] is considerably larger than those of [LnL^2]$^+$ and [LnL^3], which is related to a shorter Ln···F distance, as the geometric term present in the expression of the pseudocontact shift is proportional to $(1/r_{LnF})^3$, where r_{LnF} is the Ln···F distance.[30,49]

The longitudinal (R_1) and transverse (R_2) relaxation rates of the paramagnetic complexes studied in this work follow the trend $Gd^{3+} >> Tb^{3+} > Tm^{3+} > Yb^{3+} > Eu^{3+}$, with the values observed for the Eu^{3+} complexes being only slightly higher than those observed for the corresponding diamagnetic Lu^{3+} derivatives (Table 4). The trend observed for the lanthanide ions other than Gd^{3+} follows the order expected on the basis of their effective magnetic moments, although exceptions to this behaviour have been reported.[50] The [LnL^1] complexes present higher ^{19}F relaxation rates, while [LnL^2]$^+$ complexes show slightly higher R_1 and R_2 values than the [LnL^3] analogues.

The longitudinal ^{19}F relaxation rates of Gd^{3+} complexes are dominated by the dipolar contribution, which at the high magnetic field strengths used here (> 7 T) can be approximated by Eq (3), in which the contribution of electron relaxation has been neglected.[9]

$$R_1 = \frac{2}{15}\frac{\gamma_I^2 g^2 \mu_B^2}{r_{GdF}^6} S(S+1)\left(\frac{\mu_0}{4\pi}\right)^2 \left[\frac{7\tau_R}{1+\omega_S^2\tau_R^2} + \frac{3\tau_R}{1+\omega_I^2\tau_R^2}\right] \quad (3)$$

In this equation $\mu_0/4\pi$ is the magnetic permeability of a vacuum, S is the electron spin ($S = 7/2$ for Gd^{3+}), γ_I is the nuclear gyromagnetic ratio, g is the electron g factor, μ_B is the Bohr magneton, r_{GdF} is the nuclear-spin-electron-spin distance and ω_S and ω_I are the electron and nuclear Larmor frequencies, respectively. For Ln^{3+} ions other than Gd^{3+} R_1 presents contributions of both the dipolar and Curie spin mechanisms according to Eq (4), where μ_{eff} is the effective magnetic moment of the Ln^{3+} ion, B_0 is the magnetic field strength and τ_c is calculated according to Eq. (5) and depends on the rotational correlation time and the longitudinal electronic relaxation time (T_{1e}).

$$R_1 = \frac{2}{15}\frac{\gamma_I^2 \mu_{eff}^2 \mu_B^2}{r_{LnF}^6}\left(\frac{\mu_0}{4\pi}\right)^2 \left[\frac{7\tau_c}{1+\omega_S^2\tau_c^2} + \frac{3\tau_c}{1+\omega_I^2\tau_c^2}\right] + \frac{6}{5}\frac{\gamma_I^2 B_0^2 \mu_{eff}^4 \mu_B^4}{(3kT)^2 r_{LnF}^6}\left(\frac{\mu_0}{4\pi}\right)^2 \left[\frac{\tau_R}{1+\omega_I^2\tau_R^2}\right] \quad (4)$$

Where

$$\frac{1}{\tau_c} = \frac{1}{\tau_R} + \frac{1}{T_{1e}} \quad (5)$$

The first term in Eq (4) accounts for the dipolar interaction and the second term for the Curie spin mechanism, which becomes more important upon increasing the magnetic field strength, particularly for Ln^{3+} ions with high μ_{eff} values.[9]

The relaxation data shown in Table 4 were analysed simultaneously by using Eqs (3)-(5). The Eu^{3+} complexes were not included in the analysis due to the small paramagnetic effect observed in the relaxation rates, which are very similar to those observed for the Lu^{3+} analogues. All R_1 values were corrected for the diamagnetic contribution by using the data obtained for the Lu^{3+} complexes. The transverse relaxation rates were not included in the quantitative analysis due to their higher experimental uncertainties. The experimental data were fitted by assuming that [LnL^1] and [LnL^3] complexes present identical τ_R values and different r_{LnF} distances, which were considered independent of the Ln^{3+} ion for the complexes with a given ligand. Furthermore, the r_{LnF} distance in [LnL^2]$^+$ complexes was considered to be identical to that of [LnL^3], while the τ_R values were assumed to be different. DFT calculations support that the r_{LnF} distances do not change significantly across the lanthanide series, providing very similar values for [LnL^2]$^+$ and [LnL^3] complexes (Figure S23, Supporting Information). Finally, we hypothesized that T_{1e} and μ_{eff} values are characteristic of the particular Ln^{3+} ion, but independent of the ligand structure. This approximation is reasonable taking into account the similar coordination geometries of all the complexes studied in this work. The experimental R_1 values could be fitted reasonably well to Eqs (3)-(5) by applying these approximations, as shown in Figure 5 (see also Figure S24, Supporting Information).

Table 4. ^{19}F chemical shifts and R_1 and R_2 values for the lanthanide complexes studied in this work (5 mM in H_2O:D_2O, 9:1 v:v, pH = 7.4, 0.05 HEPES buffer).

	δ_F / ppm	R_1 / s^{-1}			R_2 / s^{-1}			T_2/T_1
		7 T	9.4 T	11.7 T	7 T	9.4 T	11.7 T	
EuL^3	-61.6	1.1	1.3	1.5	4.9	10.5	15.9	0.22
EuL^2	-61.5	1.3	1.5	1.7	10.8	12.2	14.3	0.12
EuL^1	-62.2	1.1	1.3	1.6	3.7	7.9	6.8	0.30

GdL^3	-61.3	370	357	323	435	400	416	0.85
GdL^2 [a]	-61.2	500	433	382	625	583	594	0.80
GdL^1 [a]	-62.5	1250	1152	1097	1445	1401	1417	0.87
TbL^3	-67.1	11.3	14.5	18.7	52.0	68.8	68.4	0.22
TbL^2	-69.8	15.3	18.9	22.7	67.1	71.4	82.3	0.23
TbL^1	-74.7	35.7	43.8	56.1	52.6	88.5	110	0.40
TmL^3	-58.5	5.7	7.4	9.5	26.4	33.1	82.7	0.22
TmL^2	-58.2	6.6	8.1	10.3	38.3	42.5	54.6	0.17
TmL^1	-53.9	17.2	22.3	27.2	37.2	46.9	55.2	0.46
YbL^3	-60.1	1.7	2.1	2.6	11.8	35.5	37.0	0.14
YbL^2	-59.9	1.8	2.3	2.7	11.8	20.4	39.9	0.15
YbL^1	-58.7	3.3	3.9	4.5	23.4	31.1	33.9	0.14
LuL^3	-62.2	0.8	0.9	1.0	1.5	2.1	2.8	0.53
LuL^2	-62.2	0.9	1.0	1.1	1.6	1.8	2.3	0.56
LuL^1	-63.0	0.8	0.9	0.9	5.2	6.5	9.1	0.15

[a] Data from reference 16.

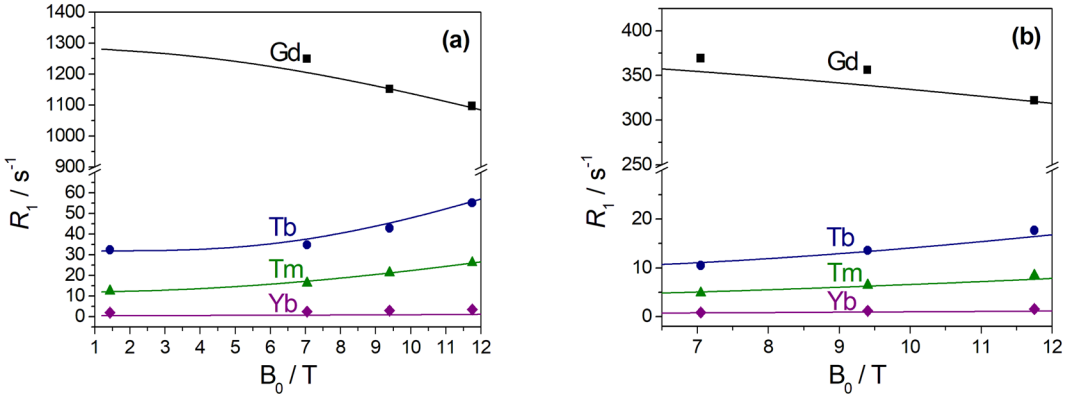

Figure 5. ^{19}F relaxation rates as a function of the magnetic field strength showing the fits and the experimental data points obtained for [LnL^1] (a) and [LnL^3] (b) (5 mM in H_2O:D_2O, 9:1 v:v, pH = 7.4, 0.05 M HEPES buffer).

Table 5. Parameters obtained from the fits of ^{19}F relaxation data.

	μ_{eff} / BM [a]	T_{1e} / fs [b]
Tb^{3+}	10.2 ± 0.3 (9.7)	720 ± 35 (203)
Tm^{3+}	8.4 ± 0.5 (7.6)	400 ± 48 (369)
Yb^{3+}	4.9 ± 4.0 (4.5)	190 ± 160 (137)
	τ_R / ps	r_{LnF} / Å
[LnL^3]	141 ± 6	9.13 ± 0.05
[LnL^2]$^+$	208 ± 10	9.13 ± 0.05
[LnL^1]	141 ± 6	7.45 ± 0.04

[a] Theoretical values are provided within parentheses. [b] In parentheses the values reported for the aqua ions (see text).

The τ_R and r_{LnF} values obtained from the fits are very similar to those obtained previously using the relaxation data of [GdL^1] and [GdL^2]$^+$ only.[16] However, the values obtained from the simultaneous fit present considerably lower standard deviations. The longer τ_R value obtained for [LnL^2]$^+$ is consistent with a larger hydrodynamic radius associated with the higher molecular weight and charge. The fitted effective magnetic moments present relatively large errors, particularly in the case of Yb^{3+}, but are close to the theoretical values.[51] The same holds for the fitted T_{1e} data, which are reasonably close to those reported for the aqua-ions,[52] providing confidence to the analysis.

The relaxation data follow the trend [LnL^1] > [LnL^2]$^+$ > [LnL^3] for Ln = Gd, Tb, Tm or Yb (Table 4). The higher R_1 values observed for [LnL^1] complexes are related to the shorter r_{LnF} distance. In the case of [LnL^2]$^+$ the longer rotational correlation time results in somewhat higher R_1 values compared with [LnL^3] (Table 5).

^{19}F MRI studies. A phantom ^{19}F MRI study at 7.05 T was performed for the series of [LnL^1] complexes to gain more precise information on their potential as fluorinated probes. The MR images were recorded using 5 mM buffered solutions of the complexes (30 mM fluorine concentration). The resulting ^{19}F MR images (Figure 6) indicated the advantageous properties of the Tb^{3+} and Tm^{3+} complexes, which present signal-to-noise ratios (SNRs) after 1 hour acquisition time of ca. 10 and 7 times higher than that of the TFA reference (Table 6). Considering that an SNR of 4-5 would be sufficient for the reliable signal detection, the complex with the most favourable properties, [TbL^1], could be detected at 20 times lower concentration than here reported, i.e. as low as 0.25 mM. Alternatively, using the acquisition time of only 10 minutes, an SNR of ~40 could be generated, while keeping the reported concentration of the complex (5 mM). In turn, these results suggest that a submilimolar concentrations of [TbL^1] in combination with fairly short acquisition times (<10 min) could be used to obtain reliable ^{19}F MRI

signals, promoting the affirmative properties of these lanthanide systems for their potential use in ^{19}F MRI.

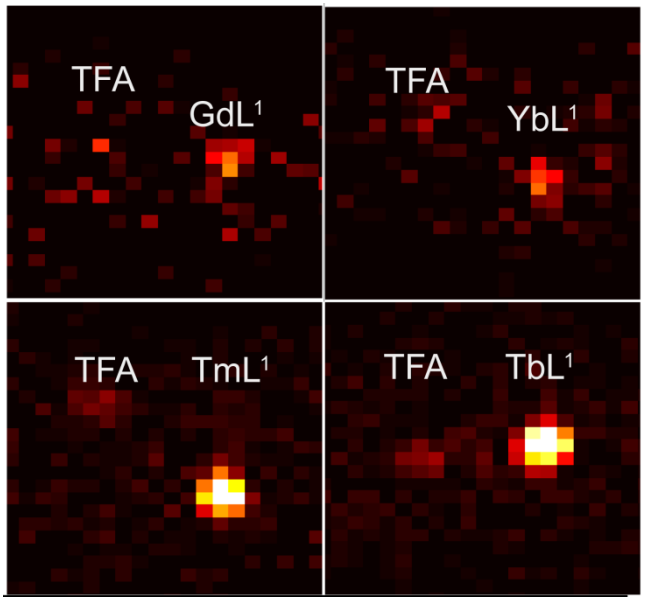

Figure 6. ^{19}F MRI on tube phantoms (5 mM complex, 7.05 T, RT) and TFA (10 mM).

On the contrary, the Yb^{3+} and Gd^{3+} complexes present SNR values similar to that of TFA, a situation that remains similar on increasing the acquisition time. These findings show that the Tb^{3+} and Tm^{3+} complexes present a good balance between the relaxation ability of the paramagnetic ion and the Ln···F distance. On the contrary, Yb^{3+} and Eu^{3+} induce very small paramagnetic relaxation enhancement to the ^{19}F signal (Table 4), resulting in a negligible SNR gain with respect to the diamagnetic reference. Finally, the dramatic T_1 relaxation enhancement induced by Gd^{3+} is accompanied by an intense shortening of T_2 (~0.7 ms at 7 T), which causes signal loss. Remarkably high SNRs were obtained previously however for $[GdL^2]^+$ with respect to the diamagnetic reference as a result of the longer Ln···F distance.[16]

Table 6. Signal to noise ratios (SNR) obtained with ^{19}F MRI studies for $[LnL^1]$ complexes using different times of acquisition (TA).

SNR	TA= 60 min	TA= 120 min	TA= 240 min
EuL^1	4.6	5.7	10.5
YbL^1	13.9	18.7	31.4
TmL^1	66.9	75.0	108.7
TbL^1	100.0	121.0	185.0
GdL^1 [a]	12.9	19.3	*B*
TFA	9.9	20.7	22.8

[a] Acquisition parameters could not be optimized due to the short T_1 and T_2 relaxation times. [b] Not determined.

CONCLUSIONS

We have shown that the properties of potential ^{19}F MRI probes can be conveniently optimized by ligand design in combination with a judicious selection of the optimal Ln^{3+} ion. The complexes investigated in this work have the advantage of providing a single major diastereoisomer in solution, which was identified as the SAP isomer by ^{1}H NMR studies in solution and single-crystal X-ray crystallography in the case of $[YbL^3]$. The complexes contain the expected inner-sphere water molecule, which results in ^{1}H relaxivities of the Gd^{3+} complexes comparable to those of commercially available contrast agents. An attractive property of the Tm^{3+} complexes is the presence of an amide resonance highly shifted with respect to bulk water, which provides a sizeable CEST signal. These amide protons are in rather fast exchange with bulk water due to the electron-withdrawing effect of the $–CF_3$ substituents. As a result, the ligand design must be improved to obtain efficient Tm^{3+} probes operating both at the ^{1}H and ^{19}F frequencies.

The detailed analysis of the ^{19}F NMR shifts and ^{19}F longitudinal and transverse relaxation rates (R_1 and R_2) allowed a very accurate determination of the average Ln···F distances in solution and the rotational correlation times associated to the Ln···F vector. The μ_{eff} and T_{1e} values obtained from the fits of the experimental data present larger uncertainties, but are still in agreement with the expected values. The Ln···F distance determined for $[LnL^1]$ complexes (7.45 $\pm$ 0.04 Å) is optimal for Ln^{3+} ions such as Tb^{3+}, as confirmed by *in vitro* MRI studies. The longer distance in $[LnL^3]$ and $[LnL^2]^+$ complexes (9.13 $\pm$ 0.05 Å) is more favourable for Gd^{3+}.

This work reports strategies leading to compounds that combine several mechanisms into a single probe, expanding the knowledge on the parameters involved in providing MRI response. While further optimization is required, for instance to improve the CEST response, the results reported here pave the way towards efficient dual-response MRI probes.

EXPERIMENTAL AND COMPUTATIONAL SECTION

Materials. DO3A*t*Bu was purchased from CheMatech (Dijon, France). Ligands H_2L^1 and H_3L^2 and 2-chloro-*N*-(4-(trifluoromethyl)phenyl)acetamide were prepared as reported previously. All other reagents and solvents were commercial and used without further purification.

General methods. High resolution electrospray-ionization time-of-flight ESI-TOF mass spectra were recorded using a LC-Q-q-TOF Applied Biosystems QSTAR Elite spectrometer in positive and negative mode. Elemental analyses were accomplished on a ThermoQuest Flash EA 1112 elemental analyser. Medium performance liquid chromatography (MPLC) was carried out using a Puriflash XS 420 instrument equipped with a reverse-phase Puriflash 15C18HP column (60 Å, spherical 15 µm, 20 g) and UV-DAD detection at 210 and 254 nm, and operating at a flow rate of 10 mL/min. Aqueous solutions were lyophilized using a Telstar Cryodos-80 apparatus.

NMR spectroscopy. ^{1}H, ^{19}F and ^{13}C NMR spectra were recorded on Bruker Avance III 300 MHz, Bruker Avance III HD 400 MHz and Bruker Avance 500 MHz spectrometers. ^{19}F chemical shifts were referenced by using sodium triflate on D_2O solvent (δ = 75.6 ppm). CEST spectra were obtained from H_2O solutions of the complexes using saturation times of 10 s. The pH of the solutions was adjusted to ~7 by adding 0.01 to 0.1 M NaOH or HCl solutions.

The ^{1}H $1/T_1$ NMRD profiles were registered on a fast field-cycling Stelar SmartTracer relaxometer (Mede, Pavia, Italy) varying the magnetic field strength from 0.00024 to 0.25 T, which corresponds to a 0.01-10 MHz proton Larmor frequency range. The instrument operates under computer control providing $1/T_1$ values with an absolute uncertainty of ± 1%. Temperature was controlled with a Stelar VTC-91 airflow heater equipped with a calibrated copper–constantan thermocouple (uncertainty of ±0.1 K). Data points in the range 20-60 MHz were additionally obtained using a Stelar Relaxometer coupled to a Bruker WP80 NMR electromagnet reconditioned for variable-field measurements (15-80 MHz proton Larmor frequency). The concentration of the complex was determined using the Bulk Magnetic Susceptibility (BMS) shift method at 11.7 T.[53] ^{17}O NMR spectra were acquired on a Bruker Avance III spectrometer (11.7 T) using a 5 mm probe and standard temperature control. Aqueous solutions of the complexes (*ca.* 6-10 mM) were enriched to reach 2.0% of the ^{17}O isotope (Cambridge Isotope). The transverse relaxation rates were measured from the signal width at half-height. Chemical shifts were corrected for the BMS contribution, which was determined using ^{t}BuOH as internal reference.[54]

MRI studies. MRI measurements were performed on a Bruker BioSpec 70/30 USR magnet (software version Paravision 5.1) using Bruker surface coil (RF SUC 300 $^{1}H/^{19}F$_20mm LIN TR). All data were acquired using the fast low angle single shot (FLASH) pulse sequence. MRI phantoms were obtained using 400 µL vials each containing 5 mM solutions of the [LnL^1] complexes (pH 7.4, 0.05 M HEPES buffer) using aqueous TFA with the same fluorine concentration as a reference in all recordings. The following parameters were used for MRI acquisition: FOV = 32 x 32, MTX = 32 x 32, slice thickness 5 mm, FA = 90 ^{0}, while TR/TE and NEX were adjusted respect to individual complex in order to result in TA = 1, 2 or 4 hours (see Table S1, Supporting Information, TA = 1 and 2 hours for [GdL^1]). The signal intensity scales were adjusted individually for each complex.

1,4,7-Tris(*tert*-butoxycarboxymethyl)- 10-((4-(trifluoromethylphenyl)acetamide)-1,4,7,10-tetraazacyclododecane (1). The cyclen derivative DO3A*t*Bu was dissolved in CH_3CN (25 mL) and $NaHCO_3$ (0.3345 g, 3.98 mmol, 5.1 eq) was added. A solution of 2-chloro-*N*-(4-(trifluoromethyl)phenyl)acetamide[16] (0.2421 g, 1.019 mmol, 1.3 eq) in CH_3CN (20 mL) was added dropwise to the mixture at ambient temperature. Once the addition was finished the mixture was heated at 46 ºC for 7 days, until the alkylation was complete. The reaction mixture was cooled to room temperature, filtered and evaporated to dryness *in vacuo*. The yellow oil was re-dissolved in CH_2Cl_2 and washed with water (20 mL). The organic layer was concentrated under reduced pressure to afford a yellowish oil. The product was purified by column chromatography on neutral alumina ($CHCl_3$ to $CHCl_3$:MeOH 95:5 (v:v)) to give a yellow foam (0.4829 g, 87%). ^{1}H NMR (300 MHz, $CDCl_3$): δ_H (ppm): 10.43 (s, 1H, NH), 8.07-8.04 (dd, 2H, CH_{Ph}), 7.43-7.40 (dd, 2H, CH_{Ph}), 3.77 (s, 2H, CH_2), 3.64-1.92 (m, 22H, CH_2), 1.63 (s, 3H, CH_3), 1.25 (s, 9H, CH_3). ^{13}C-RMN (solvent $CDCl_3$, 298 K, 75 MHz) δ_C (ppm): 172.3 (quaternary, CO), 171.9 (quaternary, CH_{Ph}), 142.0 (quaternary, CH_{Ph}), 125.3 (quaternary, CF_3), 119.9 (quaternary, CH_{Ph}), 82.2 (quaternary, CCH_3), 82.1 (quaternary, CCH_3), 57.3 (secondary, CH_2), 55.7 (secondary, CH_2), 31.9 (secondary, CH_2), 29.6 (secondary, CH_2), 29.3 (secondary, CH_2), 27.9 (primary, CH_2), 27.9 (primary, CH_2), 22.7 (primary, CH_2). ^{19}F-RMN (solvent $CDCl_3$, 298 K, 282 MHz) δ_F (ppm): -62.1 (CF_3). Mass spectrometry (ESI^+) m/z (%BPI): 738.40 (100) ($[C_{35}H_{56}F_3N_5NaO_7]^+$).

Triacetic 1,4,7-Tris(carboxymethyl)- 10-((4-(trifluoromethylphenyl)acetamide)-1,4,7,10-tetraazacyclododecane acid (H_3L^3). Compound **1** was dissolved in formic acid (5 mL) and the mixture was refluxed for 48 h. Subsequently, the acid was evaporated and the residue was dissolved in water. The solvent was again evaporated and this process was repeated five times to remove completely formic acid. The product was re-dissolved in water (10 mL) and lyophilized to provide a yellowish solid (0.2675 g, 72%). ^{1}H NMR (300 MHz, D_2O): δ_H (ppm): 8.47 (s, 2H, CH_{Ph}), 7.73-7.69 (dd, 2H, CH_{Ph}), 3.99-2.83 (m, 24H, CH_2). ^{13}C-RMN (solvent D_2O, 298 K, 75 MHz) δ_C (ppm): 172.4 (quaternary, CO), 171.0 (quaternary, CH_{Ph}), 140.3 (quaternary, CH_{Ph}), 126.3 (quaternary, CH_{Ph}), 126.3 (quaternary, CF_3), 122.8 (quaternary, CH_{Ph}), 121.2 (quaternary, CH_{Ph}), 59.5 (quaternary, CCH_3), 57.5 (secondary, CH_2), 55.1 (secondary, CH_2), 51.0 (secondary, CH_2), 49.9 (secondary, CH_2). ^{19}F-RMN (solvent D_2O, 298 K, 282 MHz) δ_F (ppm): -61.8 (CF_3). Mass spectrometry (ESI^+) m/z (%BPI): 548.23 (97) ($[C_{23}H_{33}F_3N_5O_7]^+$); 570.21 (100) ($[C_{23}H_{32}F_3N_5NaO_7]^+$), 586.18 (32) ($[C_{23}H_{32}F_3KN_5O_7]^+$); 608.16 (17) ($[C_{23}H_{31}F_3KN_5NaO_7]^+$.

General procedure for the preparation of the complexes: The corresponding ligand H_3L^1, H_3L^2 or H_2L^3 was solved in *n*-butanol in the presence of base (DIPEA) and the solution was homogenized with ultrasound bath assistance. The corresponding solid hydrated $LnCl_3$ salt (Ln = Eu, Gd, Tb, Tm, Yb or Lu) was added and the mixture was heated at 112 ºC for 6 h. Subsequently, the mixture was allowed to cool down and the solvent was removed by the use of the rotary evaporator to give an orange crude product. The complexes were purified by reverse-phase medium performance liquid chromatography (MPLC) using UV detection. For the neutral complexes MPLC purification was carried out using a gradient of solvent B (CH_3CN, 10 to 30%) in solvent A (H_2O). For the charged complexes, purification was achieved with a gradient of solvent B (0.01% HCOOH in CH_3CN, 5 to 30%) in solvent A (0.01% HCOOH in H_2O). The fractions containing the complexes were combined and the solvent was removed *in vacuo*. The final product was re-dissolved in water and lyophilized to furnish the final complexes.

EuL^1. White solid (0.0309 g, 64%). Mass spectrometry (ESI^+) m/z (%BPI): 788.10 (100) ($[C_{24}H_{28}N_5O_7F_6NaEu]^+$). HR-MS ($ESI^+$) m/z: $[M+Na]^+$, calculated: 788.0997, found: 788.0994.

GdL[1]. White solid (0.0282 g, 56%). Mass spectrometry (ESI^+) m/z (%BPI): 793.10 (100) ($[C_{24}H_{28}N_5O_7F_6NaGd]^+$). HR-MS ($ESI^+$) m/z: $[M+Na]^+$, calculated: 793.1026, found: 793.0992.

LuL[1]. White solid (0.0367 g, 43%). Mass spectrometry (ESI^+) m/z (%BPI): 810.12 (100) ($[C_{24}H_{28}N_5O_7F_6NaLu]^+$), 788.14 (7) ($[C_{24}H_{29}N_5O_7F_6Lu]^+$). HR-MS ($ESI^+$) m/z: $[M+Na]^+$, calculated: 810.1192, found: 810.1190, $[M+H]^+$, calculated: 788.1373, found: 788.1378.

TbL[1]. White solid (0.0479 g, 54%). Mass spectrometry (ESI^+) m/z (%BPI): 794.10 (100) ($[C_{24}H_{28}N_5O_7F_6NaTb]^+$). HR-MS ($ESI^+$) m/z: $[M+Na]^+$, calculated: 794.1038, found: 794.1045.

TmL[1]. White solid (0.0431 g, 63%). Mass spectrometry (ESI^+) m/z (%BPI): 804.11 (100) ($[C_{24}H_{28}N_5O_7F_6NaTm]^+$), 782.13 (12) ($[C_{24}H_{29}N_5O_7F_6Tm]^+$). HR-MS ($ESI^+$) m/z: $[M+Na]^+$, calculated: 804.1127, found: 804.1128, $[M+H]^+$, calculated: 782.1307, found: 782.1313.

YbL[1]. White solid (0.0210 g, 49%). Mass spectrometry (ESI^+) m/z (%BPI): 809.12 (100) ($[C_{24}H_{28}N_5O_7F_6NaYb]^+$), 787.14 (15) ($[C_{24}H_{29}N_5O_7F_6Yb]^+$). HR-MS ($ESI^+$) m/z: $[M+Na]^+$, calculated: 809.1152, found: 809.1173, $[M+H]^+$, calculated: 787.1354, found: 787.1362.

EuL[2]. White solid (0.0291 g, 31%). Mass spectrometry (ESI^+) m/z (%BPI): 841.17 (100) ($[C_{30}H_{34}N_6O_6F_6Eu]^+$). HR-MS ($ESI^+$) m/z: $[M]^+$, calculated: 841.1650, found: 841.1651.

GdL[2]. White solid (0.0286 g, 31%). Mass spectrometry (ESI^+) m/z (%BPI): 846.17 (100) ($[C_{30}H_{34}N_6O_6F_6Gd]^+$). HR-MS ($ESI^+$) m/z: $[M]^+$, calculated: 846.1679, found: 846.1673.

LuL[2]. White solid (0.0403 g, 51%). Mass spectrometry (ESI^+) m/z (%BPI): 863.19 (100) ($[C_{30}H_{34}N_6O_6F_6Lu]^+$). HR-MS ($ESI^+$) m/z: $[M]^+$, calculated: 863.1846, found: 863.1863.

TbL[2]. White solid (0.0517 g, 56%). Mass spectrometry (ESI^+) m/z (%BPI): 847.17 (100) ($[C_{30}H_{34}N_6O_6F_6Tb]^+$). HR-MS ($ESI^+$) m/z: $[M]^+$, calculated: 847.1692, found: 847.1698.

TmL[2]. White solid (0.0191 g, 21%). Mass spectrometry (ESI^+) m/z (%BPI): 857.18 (100) ($[C_{30}H_{34}N_6O_6F_6Tm]^+$).

YbL[2]. White solid (0.0233 g, 31%). Mass spectrometry (ESI^+) m/z (%BPI): 862.18 (100) ($[C_{30}H_{34}N_6O_6F_6Yb]^+$). HR-MS ($ESI^+$) m/z: $[M]^+$, calculated: 862.1827, found: 862.1817.

EuL[3]. White solid (0.0823 g, 62%). Mass spectrometry (ESI^+) m/z (%BPI): 720.11 (100) ($[C_{23}H_{29}N_5O_7F_3NaEu]^+$). HR-MS ($ESI^+$) m/z: $[M+Na]^+$, calculated: 720.1123, found: 720.1127.

GdL[3]. White solid (0.0591 g, 73%). Mass spectrometry (ESI^+) m/z (%BPI): 725.11 (100) ($[C_{23}H_{29}N_5O_7F_3NaGd]^+$). HR-MS ($ESI^+$) m/z: $[M+Na]^+$, calculated: 725.1152, found: 725.1139.

LuL[3]. White solid (0.0213 g, 46%). Mass spectrometry (ESI^+) m/z (%BPI): 742.13 (100) ($[C_{23}H_{29}N_5O_7F_3NaLu]^+$), 758.12 (43) ($[C_{23}H_{29}N_5O_7F_3KLu]^+$). HR-MS ($ESI^+$) m/z: $[M+Na]^+$, calculated: 742.1319, found: 742.1315.

TbL[3]. White solid (0.0705 g, 54%). Mass spectrometry (ESI^+) m/z (%BPI): 726.12 (100) ($[C_{23}H_{29}N_5O_7F_3NaTb]^+$), 704.13 (10) ($[C_{23}H_{30}N_5O_7F_3Tb]^+$). HR-MS ($ESI^+$) m/z: $[M+Na]^+$, calculated: 726.1164, found: 726.1158, $[M+H]^+$, calculated: 704.1345, found: 704.1340.

TmL[3]. White solid (0.0817 g, 61%). Mass spectrometry (ESI^+) m/z (%BPI): 736.13 (100) ($[C_{23}H_{29}N_5O_7F_3NaTm]^+$), 714.14 (10) ($[C_{23}H_{30}N_5O_7F_3Tm]^+$). HR-MS ($ESI^+$) m/z: $[M+Na]^+$, calculated: 726.1253, found: 726.1277, $[M+H]^+$, calculated: 714.1434, found: 714.1427.

YbL[3]. White solid (0.0536 g, 65%). Mass spectrometry (ESI^+) m/z (%BPI): 741.13 (100) ($[C_{23}H_{29}N_5O_7F_3NaYb]^+$), 719.15 (10) ($[C_{23}H_{30}N_5O_7F_3Yb]^+$). HR-MS ($ESI^+$) m/z: $[M+Na]^+$, calculated: 741.1300, found: 741.1295.

Crystal structure determination. A single crystal of $[YbL^3(H_2O)]\cdot 7H_2O\cdot$was analysed by X-ray diffraction. Crystallographic data were collected at 100 K using a Bruker D8 Venture diffractometer with a Photon 100 CMOS detector and Mo-Kα radiation (λ = 0.71073 Å) generated by an Incoatec high brilliance microfocus source equipped with Incoatec Helios multilayer optics. The software APEX3[55] was used for collecting frames of data, indexing reflections, and the determination of lattice parameters, SAINT[56] for integrating the intensity of the reflections, and SADABS[57] for scaling and empirical absorption correction. The structure was solved by dual-space methods using the program SHELXT.[58] All non-hydrogen atoms were refined with anisotropic thermal parameters by full-matrix least-squares calculations on F^2 using the program SHELXL-2014.[59] Hydrogen atoms were inserted at calculated positions and constrained with isotropic thermal parameters. CCDC 1891733 contains the supplementary crystallographic data for this paper. These data can be obtained free of charge from the Cambridge Crystallographic Data Centre via www.ccdc.cam.ac.uk/data_request/cif. Crystal data and structure refinement details: Formula: $C_{23}H_{45}F_3N_5O_{15}Yb$; MW: 861.68; crystal system: triclinic; space group: P–1; a=9.5512(9) Å; b=10.1528(10) Å; c=17.9472(16) Å; α= 103.418(3)°, β=99.954(3)°, γ = 96.389(3)°; V=1646.4(3) Å^3; $F(000)$=870; Z=2; D_{calc}=1.738 g cm^{-3}; μ=2.932 mm^{-1}; θ range=2.70– 30.57°; R_{int}=0.0260; 67698 measured reflections, of which 10095 were independent and 9781 were unique with $I > 2\sigma(I)$. GOF on F^2=1.049; $R1$=0.0146; $wR2$ (all data) = 0.0361; Largest differences peak and hole: 1.070 and –0.965 eÅ^{-3}.

Computational details. All the calculations were carried out by using the Gaussian 09 package (Revision D.01).[60] Geometry optimizations of the $[LnL^1(H_2O)]\cdot 2H_2O$, $[LnL^2(H_2O)]^+\cdot 2H_2O$ and $[LnL^1(H_2O)]\cdot 2H_2O$ were performed using the hybrid meta-GGA TPSSh exchange-correlation functional.[61] Two explicit second sphere water molecules were included in the model systems to improve the description of the Ln-O_{water} bonds.[22,24] Bulk solvent effects were considered by using the integral-equation

formalism variant of the polarizable continuum model (IEFPCM).[62] The large-core quasi-relativistic effective core potential (LCRECP) approach and the associated [5s4p3d]-GTO valence-basis set was employed for all lanthanides,[63] in combination with the 6–31G(d,p) basis set for ligand atoms. Geometry optimizations were followed by frequency calculations to confirm the nature of the optimized geometries as local minima.

ASSOCIATED CONTENT

^{1}H, ^{13}C, ^{19}F and ^{1}H CEST NMR spectra, bond distances and optimized geometries obtained with DFT. This material is available free of charge via the Internet at http://pubs.acs.org.

AUTHOR INFORMATION

Corresponding Authors

*E-mail:
goran.angelovski@tuebingen.mpg.de
carlos.platas.iglesias@udc.es

Author Contributions

The manuscript was written through contributions of all authors. All authors have given approval to the final version of the manuscript.

ACKNOWLEDGMENT

Authors R. P.-P., D. E.-G. and C. P.-I. thank Ministerio de Economía y Competitividad (CTQ2016-76756-P) and Xunta de Galicia (ED431B 2017/59 and ED431D 2017/01) for generous financial support and Centro de Supercomputación of Galicia (CESGA) for providing the computer facilities. R. P.-P. thanks Ministerio de Economía y Competitividad for a PhD FPI grant (BES-2014-068399) and fellowships for short term stays in Tübingen (EEBB-I-17-12213) and Alessandria (EEBB-I-18-13075). T. S. thanks the German Academic Exchange Service (DAAD) for the PhD fellowship. M.B. is grateful to Università del Piemonte Orientale for financial support (Ricerca locale 2016). This work was carried out within the framework of the COST CA15209 Action "European Network on NMR Relaxometry".

REFERENCES

(1) Holland, G. N.; Bottomley, P. A.; Hinshaw, W. S. ^{19}F Magnetic Resonance Imaging. *J. Magn. Reson.* **1977**, *28*, 133-136.

(2) McFarland, E.; Koutcher, J. A.; Rosen, B. R.; Teicher, B.; Brady, T. J. In vivo ^{19}F NMR Imaging. *J. Comput. Assist. Tomogr.* **1985**, *9*, 8-15.

(3) a) Tirotta, I.; Dichiarante, V.; Pigliacelli, C.; Cavallo, G.; Terraneo, G.; Bombelli, F. B.; Metrangolo, P.; Resnati, G. ^{19}F Magnetic Resonance Imaging (MRI): From Design of Materials to Clinical Applications. *Chem. Rev.* **2015**, *115*, 1106-1129; b) Kislukhin, A. A.; Xu, H.; Adams, S. R.; Narsinh, K. H.; Tsien, R. Y.; Ahrens, E. T. Paramagnetic fluorinated nanoemulsions for sensitivecellularfluorine-19 magnetic resonance imaging. *Nat. Mater.* **2016**, *15*, 662-668.

(4) Peterson, K. L.; Srivastava, K.; Pierre, C. C. Fluorinated Paramagnetic Complexes: Sensitive and Responsive Probes for Magnetic Resonance Spectroscopy and Imaging. *Front. Chem.* **2018**, *6,* 160.

(5) Harvey, P.; Kuprov, I.; Parker, D. Lanthanide Complexes as Paramagnetic Probes for ^{19}F Magnetic Resonance. *Eur. J. Inorg. Chem.* **2012**, 2015-2022.

(6) Kadjane, P.; Platas-Iglesias, C.; Boehm-Sturm, P.; Truffault, V.; Hagberg, G. E.; Hoehn, M.; Logothetis, N. K.; Angelovski, G. Dual-Frequency Calcium-Responsive MRI agents. *Chem. Eur. J.* **2014**, *20*, 7351-7362.

(7) (a) McMahon, M. T.; Gilad, A. A.; Bulte, J. W. M.; van Zijl, P. C. M. Chemical Exchange Saturation Transfer Imaging: Advances and Applications, Pan Stanford Publishing Pte. Ltd., Singapore, 2017; (b) Liu, G.; Song, X.; Chan, K. W. Y.; McMahon, M. T. Nuts and Bolts of Chemical Exchange Saturation Transfer MRI. *NMR Biomed.* **2013**, *26*, 810-828.

(8) Evbuomwan, O. M.; Terreno, E.; Aime, S.; Sherry, A. D. CEST and Paracest Agents for Molecular Imaging. In The Chemistry of Molecular Imaging, First Edition (Long, N.; Wong, W.-T. Eds), John Wiley & Sons, 2015.

(9) Peters, J. A.; Huskens, J.; Raber, D. J. Lanthanide Induced Shifts and Relaxation Enhancements. *Prog. Nucl. Magn. Reson. Spectrosc.* **1996**, *28*, 283-350.

(10) Schmid, F.; Höltke, C.; Parker, D.; Faber, C. Boosting ^{19}F MRI-SNR Efficient Detection of Paramagnetic Contrast Agents Using Ultrafast Sequences. *Magn. Reson. Med.* **2013**, *69*, 1056-1062.

(11) a) Chalmers, K. H.; De Luca, E.; Hogg, N. H. M.; Kenwright, A. M.; Kuprov, I.; Parker, D.; Botta, M.; Wilson, J. I.; Blamire, A. M. Design Principles and Theory of Paramagnetic Fluorine-Labelled Lanthanide Complexes as Probes for ^{19}F Magnetic Resonance: A Proof-of-Concept Study. *Chem. Eur. J.*, **2010**, *16*, 134-148; b) Chalmers, K. H.; Botta, M.; Parker, D. Strategies to Enhance Signal Intensity with Paramagnetic Fluorine-Labelled Lanthanide Complexes as Probes for ^{19}F Magnetic Resonance. *Dalton Trans.* **2011**, *40*, 904-913. c) Chalmers, K. H.; Kenwright, A. M.; Parker, D.; Blamire, A. M. ^{19}F-Lanthanide Complexes with Increased Sensitivity for ^{19}F-MRI: Optimization of the MR Acquisition. *Magn. Reson. Med.*, **2011**, *66*, 931–936. d) Senanayake, P. K.; Kenwright, A. M.; Parker, D.; van der Hoorn, S. K. Responsive fluorinated lanthanide probes for ^{19}F magnetic resonance spectroscopy. *Chem. Commun.*, **2007**, 2923–2925. e) Kenwright, A. M.; Kuprov, I.; De Luca, E.; Parker, D.; Pandya, S. U.; Senanayake, P. K.; Smith, D. G. ^{19}F NMR based pH probes: lanthanide(III) complexes with pH-sensitive chemical shifts. *Chem. Commun*., **2008**, 2514–2516.

(12) a) Jiang, Z.-X.; Feng, Y.; Yu, Y. B. Fluorinated Paramagnetic Chelates as Potential Multi-Chromic ^{19}F Tracer Agents. *Chem. Commun.* **2011**, *47*, 7233-7235. b) Srivastava, K.; Weitz, E. A.; Peterson, K. L.; Marjanska, M.; Pierre, V. C. Fe- and Ln-DOTAm-F12 Are Effective Paramagnetic Fluorine Contrast Agents for MRI in Water and Blood. *Inorg. Chem*. **2017**, *56*, 1546−1557; c) Herynek, V.; Martiniskova, M.; Bobrova, Y.; Galisova, A.; Kotek, J.; Hermann, P.; Koucky, F.; Jirak, D.; Hajek, M. Low-molecular-weight paramagnetic ^{19}F contrast agents for fluorine magnetic resonance imaging. *Magn. Reson. Mater. Phy.* **2018**, https://doi.org/10.1007/s10334-018-0721-9.

(13) a) Cakić, N.; Savić, T.; Stricker-Shaver, J.; Truffault, V.; Platas-Iglesias, C.; Mirkes, C.; Pohmann, R.; Scheffler, K.; Angelovski, G. Paramagnetic lanthanide chelates for multicontrast MRI. *Chem. Commun.* **2016**, *52*, 9224-9227; b) Cakić, N.; Tickner, B.; Zaiss, M.; Esteban-Gómez, D.; Platas-Iglesias, C.; Angelovski, G. Spectrally Undiscerned Isomers Might Lead to Erroneous Determination of Water Exchange Rates of paraCEST Eu(III) Agents. *Inorg. Chem.* **2017**, *56*, 14, 7737-7745.

(14) a) Srivastava, K.; Ferrauto, G.; Young, V. G., Jr.; Aime, S.; Pierre, V. C. Eight-Coordinate, Stable Fe(II) Complex as a Dual ^{19}F and CEST Contrast Agent for Ratiometric pH Imaging. *Inorg. Chem.* **2017**, *56*, 12206−12213; b) Blahut, J.; Hermann, P.; Gálisová, A.; Herynek, V.; Císařová, I.; Tošnerc, Z.; Kotek, J. Nickel(II) complexes of N-CH_2CF_3 cyclam derivatives as contrast agents for ^{19}F magnetic resonance imaging. *Dalton Trans.*, **2016**, *45*, 474-478; c) Yu, M.; Xie, D.; Phan, K. P.; Enriquez, J. S.; Luci, J. J.; Que, E. L. A Co^{II} complex for ^{19}F MRI-based detection of reactive oxygen species. *Chem. Commun.* **2016**, *52*, 13885-13888. d) Blahut, J.; Bernasek, K.; Galisova, A.; Herynek, V.; Cisarova, I.; Kotek, J.; Lang, J.; Matejkova, S.; Hermann, P. Paramagnetic 19F Relaxation Enhancement in Nickel(II) Complexes of N-Trifluoroethyl Cyclam Derivatives and Cell Labeling for ^{19}F MRI. *Inorg. Chem.* **2017**, *56*, 13337-13348; d) Yu, M.; Bouley, B. S.;

Enriquez, J. S.; Que, E. L. ^{19}F PARASHIFT Probes for Magnetic Resonance Detection of H_2O_2 and Peroxidase Activity. *J. Am. Chem. Soc.* **2018**, *140*, 10546-10552; e) Xie, D.; Kim, S.; Kohli, V.; Banerjee, A.; Yu, M.; Enruquez, J. S.; Luci, J. J.; Que, E. L. Hypoxia-Responsive ^{19}F MRI Probes with Improved Redox Properties and Biocompatibility. *Inorg. Chem.* **2017**, *56*, 6429-6437.

(15) a) S. Aime, S. Geninatti Crich, E. Gianolio, G. B. Giovenzana, L. Tei, E. Terreno, High sensitivity lanthanide(III) based probes for MR-medical imaging. *Coord. Chem. Rev.* **2006**, *250*, 1562-1579; b) E. Terreno, D. Delli Castelli, S. Aime, Encoding the frequency dependence in MRI contrast media: the emerging class of CEST agents. *Contrast Media Mol. Imaging* **2010**, *5*, 78-98; c) E. Vinogradov, A. D. Sherry, R. E. Lenkinski, CEST: From Basic Principles to Applications, Challenges and Oppotunities. *J. Magn. Reson.* **2013**, *229*, 155-172; d) P. C. M. van Zijl, N. N. Yadav, Chemical Exchange Saturation Transfer (CEST): What is in a Name and What Isn't? *Magn. Reson. Med.* **2011**, *65*, 927-948; e) S. J. Dorazio, J. R. Morrow, The Development of Iron(II) Complexes as ParaCEST MRI Contrast Agents. *Eur. J. Inorg. Chem.* **2012**, 2006-2014; f) P. B. Tsitovich, P. J. Burns, A. M. McKay, J. R. Morrow, Redox-activated MRI contrast agents based on lanthanide and transition metal ions. *J. Inorg. Biochem.* **2014**, *133*, 143-154; g) S. J. Ratnakar, M. Woods, A. J. M. Lubag, Z. Kovacs, A. D. Sherry, Modulation of Water Exchange in Europium(III) DOTA-Tetraamide Complexes via Electronic Substituent Effects. *J. Am. Chem. Soc.* **2008**, *130*, 6-7; h) S. J. Ratnakar, T. C. Soesbe, L. L. Lumata, Q. N. Do, S. Viswanathan, C.-Y. Lin, A. D. Sherry, Z. Kovacs, Modulation of CEST Images in Vivo by T1 Relaxation: A New Approach in the Design of Responsive PARACEST Agents. *J. Am. Chem. Soc.* **2013**, *135*, 14904-14907.

(16) a) Pujales-Paradela, R.; Savic, T.; Esteban-Gómez, D.; Angelovski, G.; Carniato, F.; Botta, M.; Platas-Iglesias, C. Gadolinium(III)-based Dual ^{1}H/^{19}F MRI Probes. *Chem. Eur. J.* **2019**, *25*, .4782-4792.

(17) Parker, D.; Puschmann, H.; Batnasov, A. S.; Senanayake, K. Structural Analysis of Nine-Coordinate Lanthanide Complexes. Steric Control of the Metal-Water Distance Across the Series. *Inorg. Chem.* **2003,** 42, 8646-8651.

(18) Aime, S.; Botta, M.; Fasano, M.; Marques, M. P. M.; Geraldes, C. F. G. C.; Pubanz, D.; Merbach, A. E. Conformational Conformational and Coordination Equilibria on DOTA Complexes of Lanthanide Metal Ions in Aqueous Solution Studied by ^{1}H-NMR Spectroscopy. *Inorg. Chem* **1997**, *36*, 2059-2068.

(19) Dale, J. Exploratory Calculations of Medium Size Rings. *Acta Chem. Scand.* **1973**, *27*, 1115-1129.

(20) (a) Milne, M.; Chicas, K.; Li, A.; Bartha, R.; Hudson, R. H. E. ParaCEST MRI contrast agents capable of derivatization via "click" chemistry. *Org. Biomol. Chem.* **2012**, *10*, 287-292. (b) Zhang, S.; Michaudet, L.; Burgess, S.; Sherry, A. D. The Amide Protons of an Ytterbium(III) dota Tetraamide Complex Act as Efficient Antennae for Transfer of Magnetization to Bulk Water. *Angew. Chem. Int. Ed.* **2002**, *41*, 1919-1921. (c) Batnasov, A. S.; Beeby, A.; Bruce, J. A.; Howard, J. A. K.; Kenwright, A. M.; Parker, D. Direct NMR and luminescence observation of water exchange at cationic ytterbium and europium centres. *Chem. Commun.* **1999**, 1011-1012.

(21) Natrajan, L. S.; Khoabane, N. M.; Dadds, B. L.; Muryn, C. A.; Pritchard, R. G.; Heath, S. L.; Kenwright, A. M.; Kuprov, I.; Faulkner, S. Probing the Structure, Conformation, and Stereochemical Exchange in a Family of Lanthanide Complexes Derived from Tetrapyridyl-Appended Cyclen. *Inorg. Chem.* **2010**, *49*, 770-7709.

(22) Regueiro-Figueroa, M.; Platas-Iglesias, C. Toward the Prediction of Water Exchange Rates in Magnetic Resonance Imaging Contrast Agents: A Density Functional Theory Study. *J. Phys. Chem. A* **2015**, *119*, 6436-6445.

(23) Thompson, A. L.; Parker, D.; Fulton, D. A.; Howard, J. A. K.; Pandya, S. U.; Puschmann, H.; Senanayake, K.; Stenson, P. A.; Badari, A.; Botta, M.; Avedano, S.; Aime, S. On the role of the counterion in defining water structure and dynamics: order, structure and dynamics in hydrophilic and hydrophobic gadolinium salt complexes. *Dalton Trans.* **2006**, 5605-5616.

(24) Esteban-Gomez, D.; de Blas, A.; Rodriguez-Blas, T.; Helm, L.; Platas-Iglesias, C. Hyperfine Coupling Constants on Inner-Sphere Water Molecules of Gd^{III}-Based MRI Contrast Agents. *ChemPhysChem*, **2012**, *13*, 3640-3650.

(25) Beeby, A.; Clarkson, I. M.; Dickins, R. S.; Faulkner, S.; Parker, D.; Royle, L.; de Sousa, A. S.; Williams, J. A. G.; Woods, M. Non-radiative deactivation of the excited states of europium, terbium and ytterbium complexes by proximate energy-matched OH, NH and CH oscillators: an improved luminescence method for establishing solution hydration states. *J. Chem. Soc., Perkin Trans. 2* **1999**, 493-503.

(26) (a) Adair, C.; Woods, M.; Zhao, P. Y.; Pasha, A.; Winters, P. M.; Lanza, G. M.; Athey, P.; Sherry, A. D.; Kiefer, G. E. Spectral properties of a bifunctional PARACEST europium chelate: an intermediate for targeted imaging applications. *Contrast Media Mol. Imaging* **2007,** 2, 55-58. (b) Polasek, M.; Kotek, J.; Hermann, P.; Cisarova, I.; Binnemans, K.; Lukes, I. Lanthanide(III) Complexes of Pyridine-N-Oxide Analogues of DOTA in Solution and in the Solid State. A Near Kind of Isomerism in Complexes of DOTA-like Ligands. *Inorg. Chem.* **2009,** 48, 466-475. (c) Dunand, F. A.; Dickins, R. S.; Parker, D.; Merbach, A. E. Towards Rational Design of Fast Water-Exchanging Gd(dota-like) Contrast Agents? Importance of the M/m Ratio. *Chem. Eur. J.* **2001,** 7 (23), 5160-5167. (d) Aime, S.; Botta, M.; Ermondi, G. NMR Study of Solution Structures and Dynamics of Lanthanide(III) Complexes of DOTA. *Inorg. Chem.* **1992,** 31 (21), 4291-4299.

(27) (a) Natrajan, L. S.; Villaraza, A. J. L.; Kenwright, A. M.; Faulkner, S. Controlled preparation of a heterometallic lanthanide complex containing different lanthanides in symmetrical binding pockets *Chem. Commun.* **2009**, 6020 –6022; (b) Nonat, A.; Regueiro-Figueroa, M.; Esteban-Gómez, D.; de Blas, A.; Rodríguez-Blas, T.; Platas-Iglesias, C.; Charbonniere, L. J. Definition of an Intramolecular Eu-to-Eu Energy Transfer within a Discrete [Eu_2L] Complex in Solution. *Chem. Eur. J.* **2012**, *18*, 8163-8173.

(28) (a) Aime, S.; Botta, M.; Ermondi, G. NMR Study of Solution Structures and Dynamics of Lanthanide(III) Complexes of DOTA. *Inorg. Chem.* **1992,** 31 (21), 4291-4299. (b) Rodriguez-Rodriguez, A.; Esteban-Gomez, D.; de Blas, A.; Rodriguez-Blas, T.; Fekete, M.; Botta, M.; Tripier, R.; Platas-Iglesias, C. Lanthanide(III) Complexes with Ligands Derived from a Cyclen Framework Containing Pyridinecarboxylate Pendants. The Effect of Steric Hindrance on the Hydration Number. *Inorg. Chem.* **2012**, *51*, 2509-2521.

(29) (a) Vipond, J.; Woods, M.; Zhao, P.; Tircso, G.; Ren, J.; Bott, S. G.; Ogrin, D.; Kiefer, G. E.; Kovacs, Z.; Sherry, A. D. A Bridge to Coordination Isomer Selection in Lanthanide(III) DOTA-tetraamide Complexes. *Inorg. Chem.* **2007**, *46*, 2584-2595. (b) Doffek, C.; Alzakhem, N.; Bischof, C.; Washner, J.; Güden-Silber, T.; Lügger, J.; Platas-Iglesias, C.; Seitz, M. Understanding the Quenching Effects of Aromatic C−H- and C−D Oscillators in Near-IR Lanthanoid Luminescence. *J. Am. Chem. Soc.* **2012**, *134*, 16413-16423 (c) Rodríguez-Rodríguez, A.; Esteban-Gómez, D.; Tripier, R.; Tircsó, G.; Garda, Z.; Tóth, I.; de Blas, A.; Rodríguez-Blas, T.; Platas-Iglesias, C. Lanthanide(III) Complexes with a Reinforced Cyclam Ligand Show Unprecedented Kinetic Inertness. *J. Am. Chem. Soc.* **2014**, *136*, 17954-17957.

(30) Bertini, I.; Luchinat, C.; Parigi, G. Magnetic Susceptibility in Paramagnetic NMR. *Prog. Nucl. Magn. Reson. Spectrosc.* **2002**, *40*, 249-273.

(31) Forsberg, J. H.; Delaney, R. M.; Zhao, Q.; Harakas, G.; Chandran, R. Analyzing Lanthanide-Induced Shifts in the NMR Spectra of Lanthanide(III) Complexes Derived from 1,4,7,10-Tetrakis(N,N-diethylacetamido)-l,4,7,l0-tetraazacyclododecane. *Inorg. Chem.* **1995**, *34*, 3705-3715.

(32) Roca-Sabio, A.; Bonnet, C. S.; Mato-Iglesias, M.; Esteban-Gómez, D.; Toth, E.-; de Blas, A.; Rodríguez-Blas, T.; Platas-Iglesias, T. Lanthanide Complexes Based on a Diazapyridinophane Platform Containing Picolinate Pendants *Inorg. Chem.* **2012**, *51*, 10893-10903.

(33) Wacker, A.; Carniato, F.; Platas-Iglesias, C.; Esteban-Gómez, D.; Wester, H.-J.; Tei, L.; Notni, J. Dimer formation of

GdDO3A-arylsulfonamide complexes causes loss of pH-dependency of relaxivity. *Dalton Trans.* **2017**, *46*, 16828-16836.

(34) (a) Goswani, L. N.; Kueffer, P. J.; Jalisatgi, S. S.; Hawthorne, M. F. Synthesis and Relaxivity Studies of a DOTA-Based Nanomolecular Chelator Assembly Supported by an Icosahedral Closo-B_{12}^{2-} -Core for MRI: A Click Chemistry Approach. *Molecules* **2013**, *18*, 9034-9048. (b) Rohrer, M.; Bauer, H.; Mintorovitch, J.; Requardt, M.; Weinmann, H.-J. Comparison of Magnetic Properties of MRI Contrast Media Solutions at Different Magnetic Field Strengths. *Invest. Radiol.* **2005**, *40*, 715-724.

(35) Wahsner, J.; Gale, E. M.; Rodríguez-Rodríguez, A.; Caravan, P. Chemistry of MRI Contrast Agents: Current Challenges and New Frontiers. *Chem. Rev.* **2019**, *119*, 957-1057.

(36) Aime, S.; Botta, M.; Esteban-Gómez, D.; Platas-Iglesias, C. Characterisation of magnetic resonance imaging (MRI) contrast agents using NMR relaxometry. *Mol. Phys.* **2019**, doi.org/10.1080/00268976.2018.1516898 .

(37) (*a*) Swift T. J.; Connick, R. E. NMR-Relaxation Mechanisms of O^{17} in Aqueous Solutions of Paramagnetic Cations and the Lifetime of Water Molecules in the First Coordination Sphere. *J. Chem. Phys.* **1962**, *37*, 307-320. (*b*) Swift T. J.; Connick, R. E. NMR-Relaxation Mechanisms of ^{17}O in Aqueous Solutions of Paramagnetic Cations and the Lifetime of Water Molecules in the First Coordination Sphere. *J. Chem. Phys.* **1964**, *41*, 2553.

(38) (a) Solomon, I. Relaxation Processes in a System of Two Spins. *Phys. Rev.* **1955**, *99*, 559-565. (b) Solomon, I.; Bloembergen, N. Nuclear magnetic interactions in the HF molecule. *J. Chem. Phys.* **1956**, *25*, 261-266. (c) Bloembergen, N. Proton relaxation times in paramagnetic solutions. *J. Chem. Phys.* **1957**, *27*, 572-573. (d) Bloembergen, N.; Morgan, L. O. Proton Relaxation Times in Paramagnetic Solutions. Effects of Electron Spin Relaxation. *J. Chem. Phys.* **1961**, *34*, 842-850.

(39) Freed, J. H. Dynamic effects of pair correlation functions on spin relaxation by translational diffusion in liquids. II. Finite jumps and independent T_1 processes. *J. Chem. Phys.* **1978**, *68*, 4034-4037.

(40) Powell, D. H.; Ni Dhubhghaill, O. M.; Pubanz, D.; Helm, L.; Lebedev, Y. S.; Schlaepfer, W.; Merbach, A. E. Structural and Dynamic Parameters Obtained from ^{17}O NMR, EPR, and NMRD Studies of Monomeric and Dimeric Gd^{3+} Complexes of Interest in Magnetic Resonance Imaging: An Integrated and Theoretically Self-Consistent Approach. *J. Am. Chem. Soc.* **1996**, *118*, 9333−9346.

(41) Mills, R. Self-Diffusion in Normal and Heavy Water in the Range 1-45º. *J. Phys. Chem.* **1973**, *77*, 685−688.

(42) Helm, L.; Merbach, A. E. Inorganic and Bioinorganic Solvent Exchange Mechanisms. *Chem. Rev.* **2005**, *105*, 1923−1959.

(43) (a) Sheth, V. R.; Li, Y.; Chen, L. Q.; Howison, C. M.; Flask, C. A.; Pagel, M. D. Measuring In Vivo Tumor pHe With CEST-FISP MRI. *Magn. Reson. Med.* **2012**, *67*, 760-768. (b) Liu, G.; Li, Y.; Sheth, V. R.; Pagel, M. D. Imaging In Vivo Extracellular pH with a Single Paramagnetic Chemical Exchange Saturation Transfer Magnetic Resonance Imaging Contrast Agent. *Mol. Imaging* **2012**, **11**, 47-57. (c) Liu, G.; Li, Y.; Pagel, M. D. Design and Characterization of a New Irreversible Responsive PARACEST MRI Contrast Agent that Detects Nitric Oxide. *Magn. Reson. Med.* **2007**, *57*, 1249-1256.

(44) Suchy, M.; Milne, M.; Elmehriki, A. A. H.; McVicar, N.; Li, A. X.; Bartha, R.; Hudson, R. H. E. Introduction of Peripheral Carboxylates to Decrease the Charge on Tm^{3+} DOTAM-Alkyl Complexes: Implications for Detection Sensitivity and in Vivo Toxicity of PARACEST MRI Contrast Agents. *J. Med. Chem.*. **2015**, *58*, 6516-6532.

(45) Zaiss, M.; Angelovski, G.; Demetriou, E.; McMahon, M. T.; Golay, X.; Scheffler, K. QUESP and QUEST Revisited – Fast and Accurate Quantitative CEST Experiments. *Magn. Reson. Med.* **2018**, *79*, 1708-1721.

(46) Ratnakar, S. J.; Viswanathan, S.; Kovacs, Z.; Jindal, A. K.; Green, K. N.; Sherry, A. D. Europium(III) DOTA-tetraamide Complexes as Redox-Active MRI Sensors *J. Am. Chem. Soc.* **2012**, *134*, 5798-5800.

(47) Lisowski, J.; Sessler, J. L.; Lynch, V.; Mody, T. D. ^1H NMR Spectroscopic Study of Paramagnetic Lanthanide(II1) Texaphyrins. Effect of Axial Ligation. *J. Am. Chem. Soc.* **1995**, *117*, 2273-2285.

(48) (a) Castro, G.; Regueiro-Figueroa, M.; Esteban-Gómez, D.; A.; Pérez-Lourido, P.; Platas-Iglesias, C.; Valencia, L. Magnetic Anisotropies in Rhombic Lanthanide(III) Complexes Do Not Conform to Bleaney's Theory. *Inorg. Chem.* **2016**, *55*, 3490-3497. (b) Funk, A. M.; Finney, K.-L. N. A.; Harvey, P.; Kenwright, A. M.; Neil, E. R.; Rogers, N. J.; Senanayake, P. K.; Parker, D. Critical analysis of the limitations of Bleaney's theory of magnetic anisotropy in paramagnetic lanthanide coordination complexes. *Chem. Sci.* **2015**, *6*, 1655-1662.

(49) (a) Forsberg, J. H.; Delaney, R. M.; Zhao, Q.; Harakas, G.; Chandran, R. Analyzing Lanthanide-Induced Shifts in the NMR Spectra of Lanthanide(III) Complexes Derived from 1,4,7,10-Tetrakis(N,N-diethylacetamido)-l,4,7,l0-tetraazacyclododecane. *Inorg. Chem.* **1995**, *34*, 3705-3715.

(50) Funk, A. M.; Harvey, P.; Finney, K.-L. N. A.; Fox, M. A.; Kenwright, A. M.; Rogers, N. J.; Senanayake, P. K.; Parker, D. Challenging Lanthanide Relaxation Theory: Erbium and Thulium Complexes That Show NMR Relaxation Rates Faster Than Dysprosium and Terbium Analogues. *Phys. Chem. Chem. Phys.* **2015**, *17*, 16507-16511.

(51) Kurzen, H.; Bovigny, L.; Bulloni, C.; Daul, C. Electronic structure and magnetic properties of lanthanide 3+ cations. *Chem. Phys. Lett.* **2013**, *574*, 129-132.

(52) (a) Alsaadi, B. M.; Rossotti, F. J. C.; Williams, R. J. P. Electron Relaxation Rates of Lanthanide Aquo-cations. *J. Chem. Soc., Dalton Trans.* **1980**, 2147-2150. (b) Bertini, I.; Capozzi, F.; Luchinat, C.; Nicastro, G.; Xia, Z. Water Proton Relaxation for Some Lanthanide Aqua Ions in Solution. *J. Phys. Chem.* **1993**, *97*, 6351-6354.

(53) Corsi, D. M.; Platas-Iglesias, C.; van Bekkum, H.; Peters, J. A. Determination of paramagnetic lanthanide(III) concentrations from bulk magnetic susceptibility shifts in NMR spectra *Magn. Reson. Chem.* **2001**, *39*, 723.

(54) K. Djanashvili, J. A. Peters, How to determine the number of inner-sphere water molecules in Lanthanide(III) complexes by ^{17}O NMR spectroscopy. A technical note. *Contrast Media Mol. Imaging* **2007**, *2*, 67-71.

(55) APEX3 Version 2016.1 (Bruker AXS Inc., 2016).

(56) SAINT Version 8.37A (Bruker AXS Inc., 2015)

(57) SADABS Version 2014/5 (Sheldrick, Bruker AXS Inc.)

(58) SHELXT Version 2014/5. G. M. Sheldrick, Acta Cryst., 2015, A71, 3-8.

(59) SHELXL Version 2014/7. G. M. Sheldrick, Acta Cryst., 2008, A64, 112-122.

(60) Gaussian 09, Revision A.01, Frisch, M. J.; Trucks, G. W.; Schlegel, H. B.; Scuseria, G. E.; Robb, M. A.; Cheeseman, J. R.; Scalmani, G.; Barone, V.; Mennucci, B.; Petersson, G. A.; Nakatsuji, H.; Caricato, M.; Li, X.; Hratchian, H. P.; Izmaylov, A. F.; Bloino, J.; Zheng, G.; Sonnenberg, J. L.; Hada, M.; Ehara, M.; Toyota, K.; Fukuda, R.; Hasegawa, J.; Ishida, M.; Nakajima, T.; Honda, Y.; Kitao, O.; Nakai, H.; Vreven, T.; Montgomery, Jr., J. A.; Peralta, J. E.; Ogliaro, F.; Bearpark, M.; Heyd, J. J.; Brothers, E.; Kudin, K. N.; Staroverov, V. N.; Kobayashi, R.; Normand, J.; Raghavachari, K.; Rendell, A.; Burant, J. C.; Iyengar, S. S.; Tomasi, J.; Cossi, M.; Rega, N.; Millam, N. J.; Klene, M.; Knox, J. E.; Cross, J. B.; Bakken, V.; Adamo, C.; Jaramillo, J.; Gomperts, R.; Stratmann, R. E.; Yazyev, O.; Austin, A. J.; Cammi, R.; Pomelli, C.; Ochterski, J. W.; Martin, R. L.; Morokuma, K.; Zakrzewski, V. G.; Voth, G. A.; Salvador, P.; Dannenberg, J. J.; Dapprich, S.; Daniels, A. D.; Farkas, Ö.; Foresman, J. B.; Ortiz, J. V.; Cioslowski, J.; Fox, D. J. Gaussian, Inc., Wallingford CT, 2009.

(61) Tao, J. M.; Perdew, J. P.; Staroverov, V. N.; Scuseria, G. E. Climbing the Density Functional Ladder: Nonempirical Meta-Generalized Gradient Approximation Designed for Molecules and Solids. *Phys. Rev. Lett.* **2003**, *91*, 146401.

(62) Tomasi, J.; Mennucci, B.; Cammi, R. Quantum mechanical continuum solvation models. *Chem. Rev.* **2005**, *105*, 2999–3093.

(63) Dolg, M.; Stoll, H.; Savin, A.; Preuss, H. Energy-adjusted pseudopotentials for the rare earth elements. *Theor. Chim. Acta* **1989**, *75*, 173-194.